

A Dual Differential Interferometer for Measurements  
of Broadband  
Surface Acoustic Waves

by

Tyson Mapp Turner

Thesis submitted to the Graduate Faculty of the  
Virginia Polytechnic Institute and State University  
in partial fulfillment of the requirements for the degree  
of

MASTER OF SCIENCE

in

Electrical Engineering

APPROVED:

---

Dr. R. O. Claus

---

Dr. A. A. Beex

---

Dr. A. A. Riad

---

Dr. W. L. Stutzman

March, 1982  
Blacksburg, Virginia

## ACKNOWLEDGEMENT

I wish to thank my advisor, Dr. Richard O. Claus, for his time, patience and encouragement. I would like also to extend special thanks to my graduate committee, Dr. A. A. Beex, Dr. A. A. Riad and Dr. W. L. Stutzman, for their comments and suggestions.

My appreciation also goes to Lynn Swanson, who helped type the text, Dan Dockery, John Gray, Janet Wade, Sam Zerwekh and especially Avinash Garg who provided many hours of help and numerous suggestions.

I must include a special note of gratitude to my mother, Mary Jane Turner, for her unfaltering encouragement and financial assistance throughout this endeavor. Lastly, I wish to thank my wife, Mary Jo, for her love and assistance.

## TABLE OF CONTENTS

ACKNOWLEDGEMENT . . . . .	ii
Chapter	page
I. INTRODUCTION . . . . .	1
1.1. Characterization of Acoustic Emission . . .	1
1.2. Overview of NDE Techniques and SAW Detection Methods . . . . .	5
1.2.1. Noncontact Transducers . . . . .	5
1.2.2. Optical Techniques . . . . .	12
1.3. Report Overview . . . . .	30
II. THEORETICAL DEVELOPMENT OF SURFACE ACOUSTIC WAVES .	33
2.1. A Mathematical Description of Surface Acoustic Waves . . . . .	33
2.2. Surface Wave Generation from Bulk Body Acoustic Emission . . . . .	45
2.3. Use of Surface Waves in Bond Evaluation . .	50
III. THE DIFFERENTIAL INTERFEROMETER . . . . .	63
3.1. Development of the Differential Interferometer Concepts . . . . .	63
3.2. Detection Limitation of the Differential Interferometer . . . . .	82
IV. THE DUAL DIFFERENTIAL INTERFEROMETER . . . . .	85
4.1. Theoretical Development of the Dual Differential Interferometer . . . . .	85
4.2. Optical Configuration of the Dual Differential Interferometer . . . . .	88
V. CONSTRUCTION OF THE DUAL INTERFEROMETRIC SYSTEM AND EXPERIMENTATION . . . . .	95
VI. CONCLUSIONS AND FOR FURTHER CONSIDERATION . . . .	104
REFERENCES . . . . .	109

## LIST OF TABLES

Table	page
1. ESAT and EMAT Performance Characteristics . . . . .	11

## LIST OF FIGURES

FIGURE	PAGE
1.1 Electrostatic Transducer . . . . .	8
1.2 Electromagnetic Transducer . . . . .	10
1.3 Optical Knife-Edge Technique . . . . .	15
1.4 Surface Profiles Using Knife-Edge . . . . .	18
1.5 Bragg-Cell Heterodyne System . . . . .	20
1.6 Optical Bragg-Cell Beam Steering . . . . .	21
1.7 Saw Optical Diffraction . . . . .	24
1.8 Fabry-Perot SAW Detection . . . . .	26
1.9 Fabry-Perot Optical Diffraction . . . . .	27
1.10 Fabry-Perot Interference Pattern . . . . .	28
1.11 Differential Interferometer . . . . .	31
2.1 Differential Particle Displacement . . . . .	35
2.2 Surface Coordinate System . . . . .	41
2.3 SAW Particle Displacements . . . . .	45
2.4 Bulk Wave Modes . . . . .	47
2.5 AE Incident on Free Surface . . . . .	48
2.6 Shear Wave Decomposition on Surface . . . . .	51
2.7 Shear Wave Coupling into Surface Coupled Pressure Wave . . . . .	52
2.8 Stoneley Wave Boundary Evaluation . . . . .	55
2.9 Clear Drilled Hole Simulating Defect . . . . .	57
2.10a Attenuation of Pitch-Catch Configuration . . . . .	58
2.10b Pulse-Echo Attenuation . . . . .	59

2.11	Progressively Drilled Hole . . . . .	60
2.12	Pitch-Catch as a Function of Depth . . . . .	61
3.1	Dual Beam Optical Geometry . . . . .	66
3.2	Angular Incidence of Dual Beams . . . . .	67
3.3	Intensity Versus Position on Ronchi Grid . . . . .	72
3.4a	Optical Geometry For Maximum Sensitivity . . . . .	73
3.4b	Narrowband Differential Interferometry . . . . .	74
3.5	Optical Set-up For Differential Interferometry . .	77
3.6	Sensitivity Bandwidth Plots . . . . .	79
3.7	Frequency Limitation of Differential Interferometer . . . . .	81
3.8	Differential Interferometer Angular Sensitivity .	84
4.1	Dual Interferometer Focus Point Geometry . . . . .	86
4.2	Nonsymmetrical Point Geometry . . . . .	89
4.3	Focus Spot Pair Polarization . . . . .	91
4.4	Dual Differential Interferometer Optical Set-up .	92
5.1	Dual Differential Interferometer Optical Set-up .	97
5.2	Optical Bench Acoustical Sensitivity . . . . .	98
5.3	Large Amplitude, Single Channel Acoustic Signal	103

## I. INTRODUCTION

### 1.1. CHARACTERIZATION OF ACOUSTIC EMISSION

Mechanical structures may fail as a consequence of stress and time-in-use. In general, the possible combinations of stress amplitude and time duration required to induce failure vary for each considered material and structural design as well as between duplicates of the same material structure. The structural integrity over reasonable component lifetimes may be determined in some cases by simple visual inspection while the structure is subjected to rated loads. However, the materials processing and construction of identical structures are not consistent [1,2,3]. Thus, the reliability of one mechanical structure chosen at random can at best be approximated only through correlation studies of a number of similar structures unless the chosen structure is individually monitored during use and parameters thought to be related to failure are observed. From these observations, it is anticipated that reliability versus time-in-use curves may be determined for a structure from its present and past work loads rather than by assuming an averaged relationship among a random selection of similar structures.

The key to the testing procedure is the determination of the physical parameters that characterize mechanical failure and the development of testing techniques to monitor these parameters. At present, theoretical descriptions of mechanical failure mechanisms are limited to considerations of homogeneous or simple layered media which contain idealized faults or fractures [1]. The fractures are modeled as penny shaped voids or inclusions which open to wedges when stressed, emitting Heaviside step function acoustic impulses which propagate through the media. Experience and experimentation have shown that prior to mechanical failure, microfractures develop and are accompanied by the generation of ultrasonic acoustic wave pulses which are created by the localized release of residual stress [1,2,3]. This wave generation process during stress is termed acoustic emission (AE). Theory suggests that the amplitude, duration, frequency of occurrence, spectral content, and direction of propagation of AE pulses may be used concurrently to determine the mechanical age and projected lifetime of a structure [1,2,3].

Longitudinal and shear acoustic waves produced by an AE event, which occurs in the bulk of a material, propagate to the material surfaces and produce a surface deformation [1,2,3]. Although the physical mechanisms responsible for



the generation of the two wave components are not well understood, the resulting surface deformation may be detected by a variety of techniques which are outlined below. Specific investigations of the microscopic phenomena responsible for AE are complicated by the distortion of the emitted acoustic waves which occurs during propagation through the material and by the general inability of surface displacement sensors to accurately pinpoint AE sources for subsequent microscopic examination. Furthermore, the different types of potential AE generation mechanisms are numerous and it has not been established which of these are related to imminent catastrophic failure [1].

Acoustic emission events occur at random within a specimen but are observed as transient, broadband particle displacements throughout the specimen's surface. Accurate characterization of an AE event necessitates the three-dimensional point specification of the surface displacement vector, [4]. but at present no single detector can resolve the three displacement components of surface particle motion simultaneously. Because experiments which use approximated idealizations of AE events having axial or spherical symmetry agree well with theory for the normal component, it is assumed that the other components

likewise agree. However, this assumed symmetry may not exist in general and conventional measurements of the surface effects related to AE may not give a true indication of actual wave propagation.

Current research also suggests that second and third order acoustic effects within the AE waveforms contain considerable information concerning the type, size, and growth rate of the microfractures responsible for AE generation [1,4]. To accurately measure these nonlinear effects, the sensitivity and selectivity of acoustic detectors must be extended.

AE observation can be made by several detection techniques including piezoelectric transducers, noncontact capacitive and electromagnetic transducers, and optical methods. All contact and electromagnetic transducers, as well as some optical techniques, inherently integrate the particle motions generated by a surface acoustic wave (SAW) coupled from an AE event over the active area of the transducer element. The surface motion on a point-by-point basis must then be deconvolved from the recorded signal. Several optical methods, however, provide point-by-point analysis of surface displacements and may retain phase information without extensive post-detection analysis. In addition, optical techniques do not load the sur-

face which avoids compounding the signal dispersion due to propagation through the material with wave distortion at the surface. Optical methods are generally based on 1) simple modulated deflection of a narrow beam due to time varying surface deformations (simple probing), 2) Fabry-Perot interferometry techniques, or 3) heterodyning of two or more probing and reference beams [5,6]. Although each method may be used to determine the amplitude of surface displacements, Fabry-Perot interferometric and heterodyning techniques have greater sensitivity and can detect SAW phase as well. Although the absolute minimum detectable SAW amplitude for these techniques is in the sub-angstrom range, generally less than  $10^{-3}$  Å, optical methods have only been applied to the measurement of normal surface displacements at present.

## 1.2. OVERVIEW OF NDE TECHNIQUES AND SAW DETECTION TECHNIQUES

### 1.2.1. Noncontact Transducers

Noncontact transducer types offer several advantages over contact transducers which include 1) the ability to

temperatures, 3) sense fields at a distance, 4) establish reproducible coupling, and 5) require no clean-up operations [7]. These advantages are tempered, however, by the relatively low coupling efficiencies of noncontact transducers in comparison to piezoelectric contact transducers. In application, therefore, trade-offs arise dependent on specific testing requirements.

A category of noncontact transducer is the electrostatic. The electrostatic transducer is an electrically modulated capacitor where the specimen is utilized as a ground plane for a capacitive plate, rigidly elevated and parallel to the specimen surface, connected to a modulation source. The mechanical stress developed at the surface  $\sigma$  is proportional to the square of the electrostatic field between the two plates and is given by [7]

$$\sigma = \epsilon_0 E^2/2, \quad (1.1)$$

where  $\epsilon_0$  is the permittivity of free space. The dynamic stress developed by superimposing a modulated field  $E_\omega$  at frequency  $\omega$  on the static field can be shown to be

$$\sigma_\omega = \epsilon_0 E_0 E_\omega. \quad (1.2)$$

This harmonic surface stress generates dilatational bulk wave modes propagating with frequency  $\omega$ . The amplitude is given by

$$u_{\omega} = \frac{\epsilon_0 E_{\omega} E_0}{\omega p v}, \quad (1.3)$$

where  $p$  and  $v$  are the material density and dilatational bulk wave velocity. A matching receiving transducer will generate an open circuit signal voltage of

$$V_{\omega} = \frac{2 \epsilon_0 E_{\omega} E_0^2}{\omega p v} \quad (1.4)$$

at the point of detection.

Cantrell and Breazeale developed a capacitive bulk wave transducer to measure second and third order effects in bulk wave propagation for accurate evaluation of material properties [7]. A schematic of the device is shown in Figure 1.1. Although signal analysis of the received signal is required due to the nonlinear properties of the device, the sensitivity is excellent. Accurate measurements of the second and third order elastic constants as well as acoustic emission have been performed.

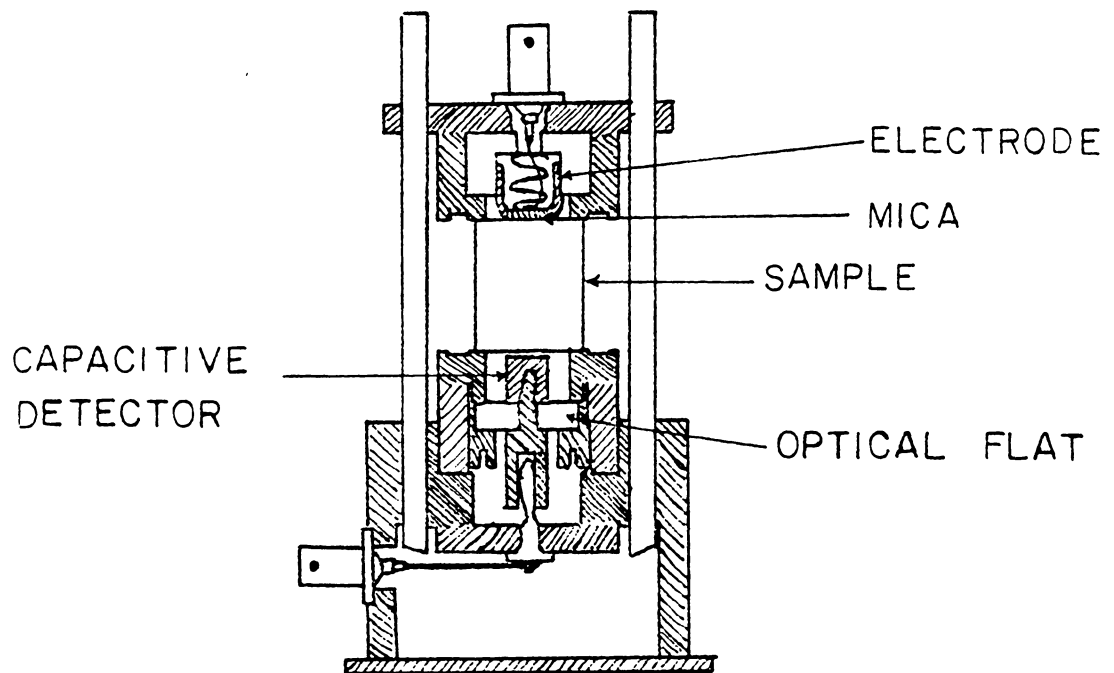


Figure 1.1. Electrostatic drive and receive system for precise ultrasonic measurements [7].

A second noncontact transducer class involves electromagnetic techniques. The principle of operation in this class is to bring a dynamic current carrying wire close to the surface of a conducting material in order to induce eddy currents within the material. Impedance changes which occur in the source coil are induced by cracks and defects within the surface layer of the conducting material, changing the resistivity of the test material. If, in addition to the source coil, a static magnetic field is present, the Lorentz force acting on the moving eddy current electrons induces a mechanical force on the material lattice. Particular orientations of the source coil can thus be used to generate dilatational or shear wave bulk propagation within the material. A similar reaction occurs in ferromagnetic materials because magneto-strictive stresses can be produced by modulation of the static magnetic field. A diagram of an electromagnetic acoustic transducer is shown in Figure 1.2 [8]. The current directions are important for the appropriate wave mode generation. These devices can also be configured for acoustic wave detection. In Table 1.1 is given a comparison between electro-static (ESAT) and electro-magnetic (EMAT) acoustic techniques [7].

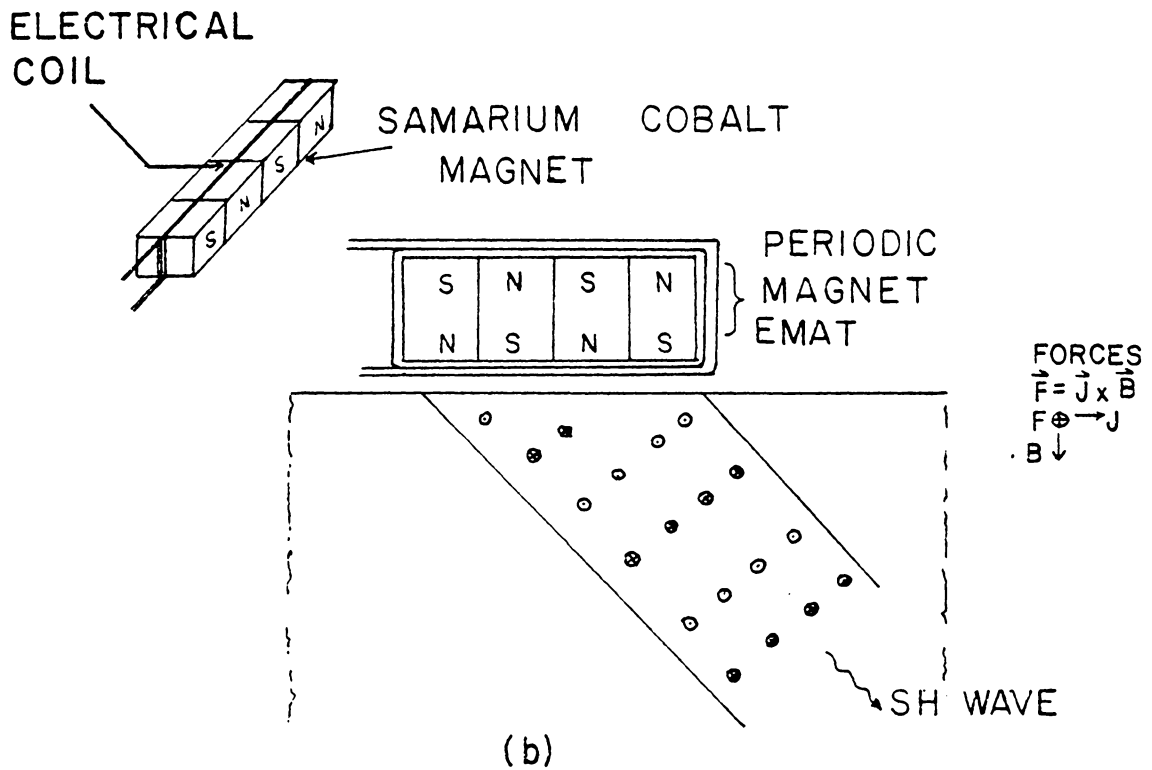
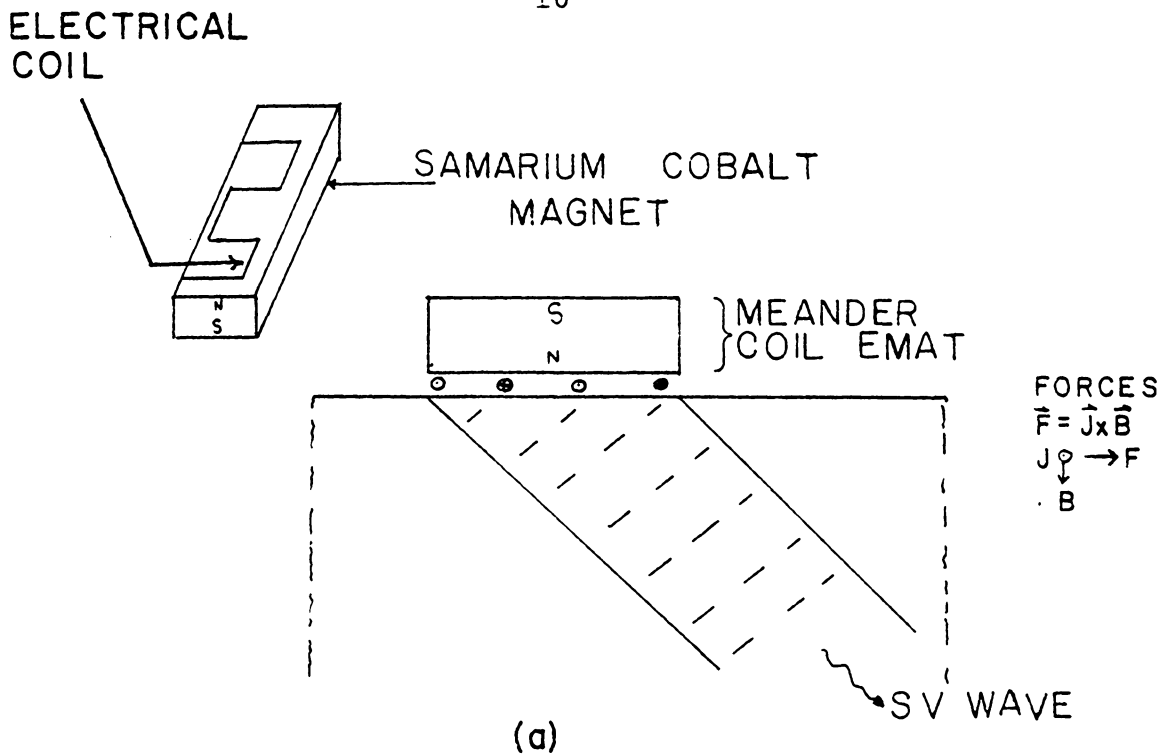


Figure 1.2. EMAT transducers with (a) meander coil to excite vertically polarized shear waves and (b) periodic magnet to excite horizontally polarized shear waves [8].



TABLE 1

## ESAT and EMAT Performance Characteristics

<u>ESAT</u>	<u>EMAT</u>
Longitudinal Stresses	Longitudinal and Shear Waves
Uniform Fields Excited	Bulk Modes Have Complex Mode Patterns
Low Impedance	High Impedance
Metal Plate and Battery	Coil and Magnet
Operate on Metal and	Operate on Metal & Magnetic
$z^{-1}$ Ceramics	Materials
$z^{-1}$ Lift-off	$e^{-az}$ Lift-off
Polished Surfaces	Rough Surfaces
High Temp Operation	High Temp Operation
Broadband	Broadband
Absolutely Calibrated	Absolutely Calibrated
Low Efficiencies	Low Efficiencies

### 1.2.2 Optical Techniques

Optical transducers are also in the family of noncontact transducers and offer similar advantages over contact transducers like the electrostatic and electromagnetic acoustic transducers. In addition, optical techniques have the unique ability to probe entire surface structures (and bulk properties of translucent materials) with simple optical geometries at real time rates. This scan rate allows entire silicon wafers, protoboards or any flat surface to be tested for cracks, delaminations and subsurface fractures quickly rather than statistically spot checked or tediously investigated point-by-point.

Optical methods have other versatile features which enhance their applications. Most optical techniques can be calibrated for particular SAW propagation directions which allows selectivity between incident waves and diffracted wave patterns when observing material defects. Also, these measurements can be absolutely calibrated relatively easily because of the linearity found in optical detection systems. Lastly, the detection system is passive in that no externally induced currents or static electromagnetic fields are required for acoustic detection. This leaves the specimen in a more natural state than with other techniques.

Two classes of optical techniques have developed dependent on the size of the optical probe beam diameter relative to acoustic wavelength [5,6]. Long wavelength scattering, or Rayleigh scattering techniques, where the probe diameter is much smaller than the acoustic wavelength, have arisen based on detection of specific physical deformations such as normal wave amplitude, surface slope and periodic reflected beam focusing and defocusing related to surface wave curvature. In the short wavelength class, the optical beam can be many times the acoustic wavelength and will, upon reflection, decompose into spatially and/or temporarily periodic phase patterns in the far field which are similar to the diffraction patterns of a phase grating.

The long-wavelength techniques in general require much simpler implementations. For example, the knife edge technique developed by Korpel, Adler and Desmares [6,7,9] is shown schematically in Figure 1.3. The laser beam incident on the surface is reflected at an angle related to the relative slope of the surface due to the surface wave. In the static case, half the reflected beam power is focused on the detector, the other half is stopped by a knife edge placed before the focusing lens. When the surface is modulated, the reflected beam is angularly modu-

lated, giving amplitude and phase information in the power passing the knife edge.

The modulation angle  $\theta_m$  of the reflected beam from the static reflection angle is given by

$$\theta_m = (2\pi / \Lambda) \delta \cos(\omega t + \phi) \quad (1.5)$$

where  $\Lambda$  is the acoustic wavelength,  $\delta$  is the normal surface wave amplitude,  $\omega$  is the acoustic wave frequency and  $\phi$  is an arbitrary phase angle. The signal power at the detector is given by

$$P_{sig} = P_0 (f_1/D) (4\pi / \Lambda) \delta \cos(\omega t + \phi) \quad (1.6)$$

where  $f_1$  is the focal length of lens 1,  $P_0$  is the laser power and  $D$  is the distance from scanner to specimen surface. A square laser beam will have at the surface a  $\sin x/x$  distribution with maximum intensity pattern spacing on the surface of

$$2d = 2(\lambda/D) f_1 \quad (1.7)$$

The maximum signal output will occur when  $d = \Lambda/2$  and thus the maximum signal at the detector can be expressed as

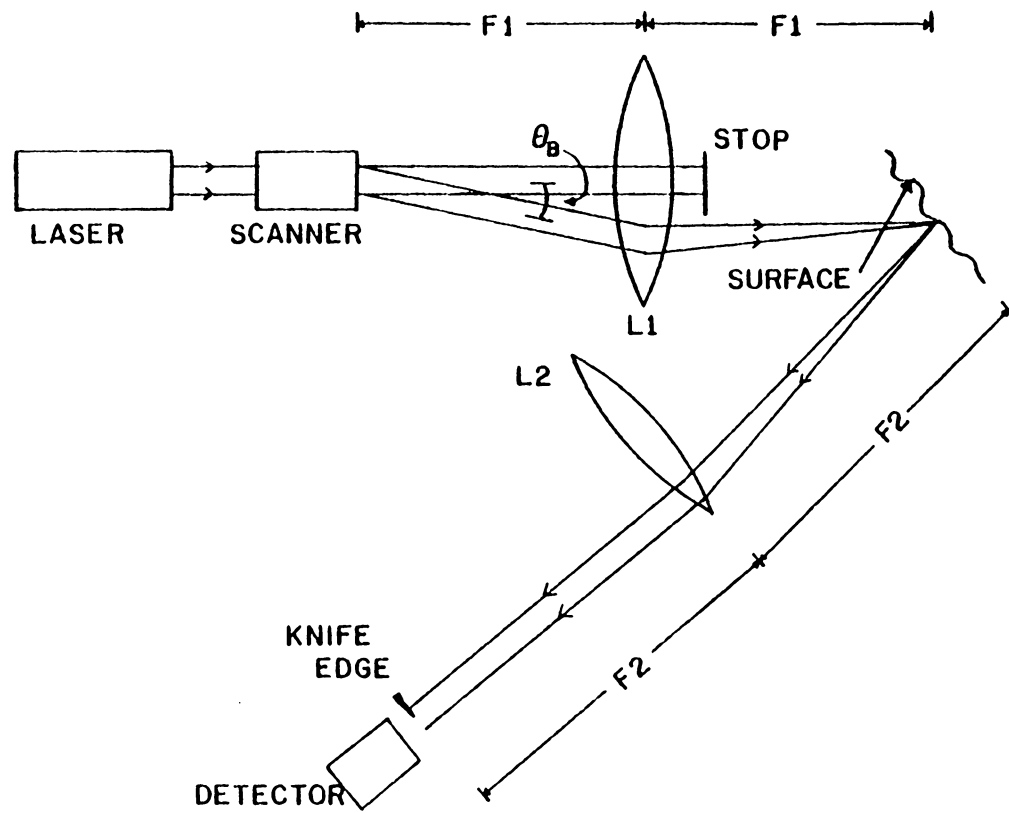


Figure 1.3. A knife-edge technique for analysis of surface wavefront propagation [6].

$$P_{\text{sig max}} = P_0 (2\pi\delta / \lambda) \cos \omega_0 t \quad (1.8)$$

where  $\lambda$  is the optical wavelength. If the detector is assumed to have quantum efficiency  $\alpha$  in amperes per watt of optical power, the signal current is given by

$$I_s = \alpha P_{\text{sign}} \quad (1.9)$$

with the RMS noise of

$$I_n = [2eB \alpha (P_0/2)]^{1/2}. \quad (1.10)$$

Equating the signal-to-noise power ratio to one, the minimum detectable signal is expressed as

$$\delta_{\text{min}} = (2eB/\alpha P_0)^{1/2} (\lambda/2\pi) \quad (1.11)$$

where  $e$  is electron charge and  $B$  is the detector bandwidth. This system was adapted to real-time visualization of the reflecting surface by scanning the optical probe across the surface with driven mirror oscillators. The laser probe location was synchronized to an oscilloscope display with  $x$  and  $y$  signals proportional to the laser position. The  $z$ -axis intensity of the oscilloscope beam

was modulated by the output signal of the optical detector. The system gave excellent results, examples of which are shown in Figure 1.4 [10]. Notice that the selectable sensitivity of group velocity direction allows detection of both incident and reflected acoustic wave patterns shown in Figures 1.4e and 1.4f.

Optical interferometry is widely used as a technique for the measurement of normal surface displacements but also allows both amplitude and phase detection. Several interferometric configurations have been developed. The first described here is an optical heterodyne system [5,6,11] in which the acoustically modulated probe beam reflected off the specimen surface is heterodyned with a reference beam at a shifted optical frequency of  $f_o \pm f_s$  where  $f_o$  is the optical source frequency and  $f_s$  is the shift frequency. If the acoustic field has modulation frequency  $f_m$  ( $f_m \neq f_s$ ), then the detectable beat frequencies at the point of recombination would be  $f_s$  ( $f_s \neq f_m$ ). The normal displacement of the acoustic wave is proportional to the amplitude of the beat signal, or the square root of the intensity. Phase information is lost in intensity measurements. Similar to the previously described visual acoustic scanner, this technique has been adopted for x-y acoustic field mapping.

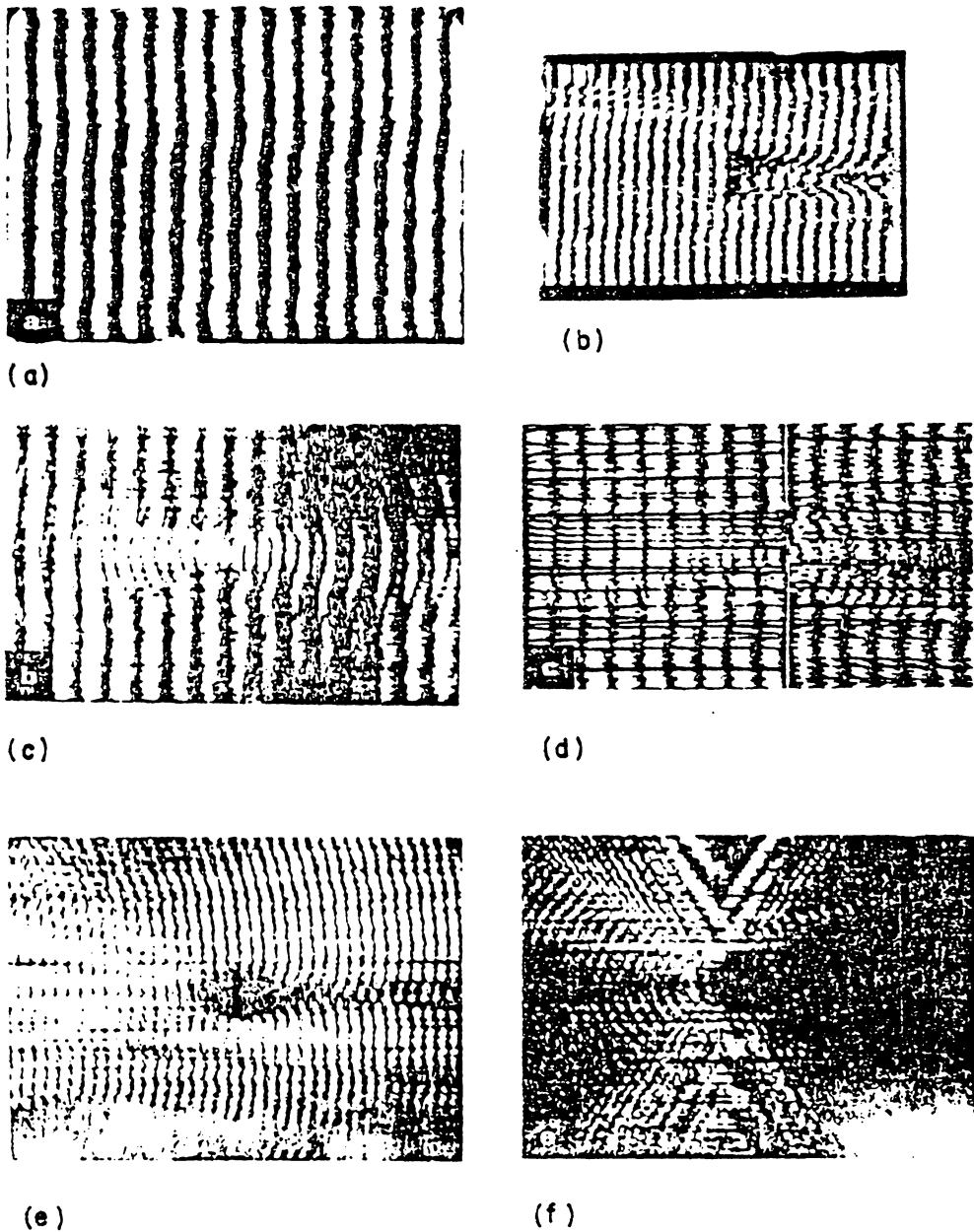


Figure 1.4. Surface scans generated by knife-edge technique of (a) a no defect substrate, (b) a rectangular cut surface notch, (c) an etched hole on the underside of a plate, (d) a washer bonded to the underside of a plate, (e) a clear drilled hole and (f) the perpendicular system orientation showing wave scatter from the drilled hole in (e) [10].



An example of a heterodyne technique is shown in Figure 1.5 [11]. The frequency shifted beam is obtained by using a Bragg water cell. The Bragg cell and associated optical field deflections are shown in Figure 1.6. The propagating acoustic water wavefront creates parallel planes of refractive index change which refract a portion of the incident light along an angled trajectory with an associated frequency shift. The undeflected beam is not changed in frequency. This effect occurs for any optical propagation direction through the cell.

Following Figure 1.5, the laser probe beam propagated through the Bragg cell and was split into two beams, one frequency shifted and deflected and one unshifted. The frequency shifted beam reflects off a reference mirror and returns to the cell. The unshifted beam is focused onto the specimen surface and reflected back to the Bragg cell. A percentage of the reference beam passes through the cell and an equal percentage of the probe beam is frequency shifted by the cell and travels along the reference beam's path since both beams have passed through the cell twice. The interfering beams have three beat frequencies,  $2f_s$  and  $2f_s + f_n$ . Using a phase sensitive detection network, the theoretical minimum detectable signal, shot-noise limited, is  $8 \times 10^{-5} \text{ A}$ . The actual observed minimum amplitude is  $2 \times 10^{-3} \text{ A}$ .

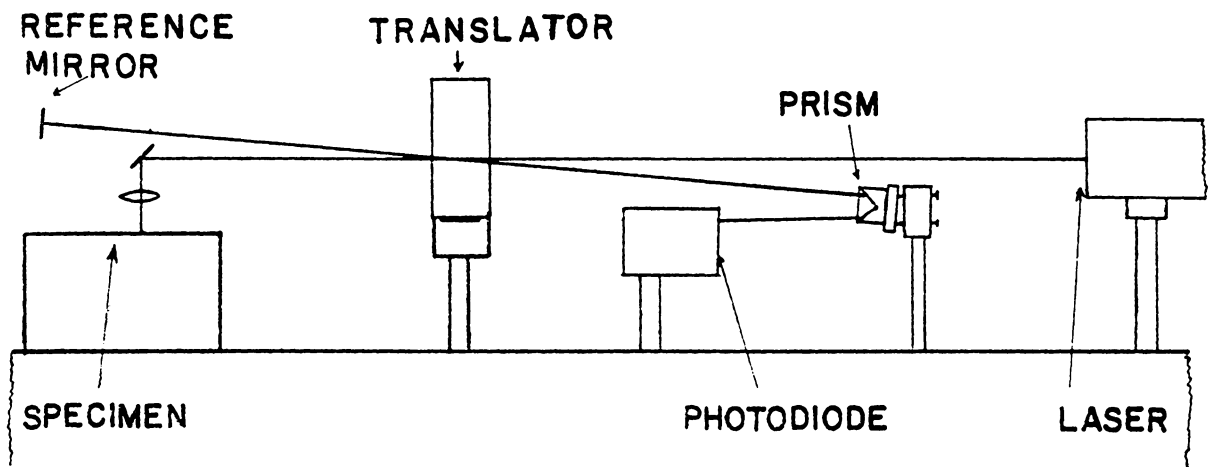


Figure 1.5. Experimental configuration of optical heterodyne system [11].

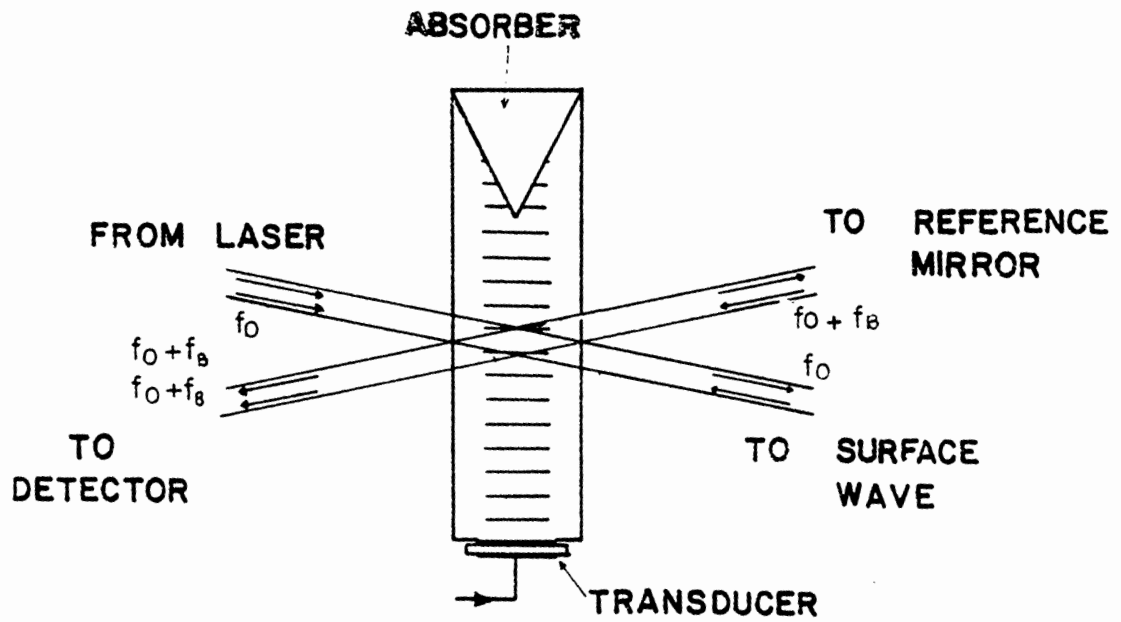


Figure 1.6. Bragg-cell double-transit beam-splitter system [11].

If the surface of the specimen is illuminated by a large diameter probe, the reflected field contains a diffraction pattern [5,12]. For small surface wave amplitude in comparison to , the optical wavelength, the  $\pm 1^{\text{st}}$  order beams will appear. In the near field, the orders will overlap with an apparent phase difference of [12]

$$\Delta\phi = z \left( \lambda / \Lambda^2 \right) \pi \quad (1.12)$$

where  $z$  is the distance from the surface in Figure 1.7. When  $\phi = (N+1/2)$  ,  $n=0,1,2,\dots$ , the optical image appears as an amplitude corrugation. The values of  $z$  for these cases are

$$z_n = (n+1/2) \left( \Lambda^2 / \lambda \right). \quad (1.13)$$

The optimal case is for  $n=0$  where the orders have greatest overlap. Here the fractional spatial amplitude modulation is

$$m_p = 4 \pi \left( \delta / \lambda \right) \quad (1.14)$$

where  $\delta$  is the normal surface displacement. This results in the signal power at the detector of

$$P_{\text{sig}} = \{ (N - 1/2) / N \}^2 (mp/\pi) P_0 \cos \omega_m t \quad (1.15)$$

where  $P_0$  is the incident laser power and  $N$  is the number of spatially filtered fringes focused on the receiver. Using a detector with quantum efficiency  $\alpha$  in amperes per watt and having bandwidth  $B$ , the minimum detectable signal defined by signal-to-noise ratio of one is given by [12]

$$\delta_{\text{min}} = (2eB/\alpha P_0)^{1/2} (\lambda/8) \{N/(N - 1/2)\} \quad (1.16)$$

where  $e$  is the electric charge in coulombs. There is seen to be little difference between this phase grating technique and the knife edge approach.

Fabry-Perot interferometers have been employed to characterize surface acoustic waves. The geometry required for achieving multiple interference severely limits the possible applications of the device. A simplified diagram of a Fabry-Perot interferometer is shown in Figure 1.8 [5]. The operating principle behind this interferometer is the development of multiple reflections, as shown in Figure 1.9, [13] which at particular angles constructively and destructively interfere to form a circular intensity pattern as shown in Figure 1.10 [13]. The two partially reflective plates must be parallel with reflection effici-

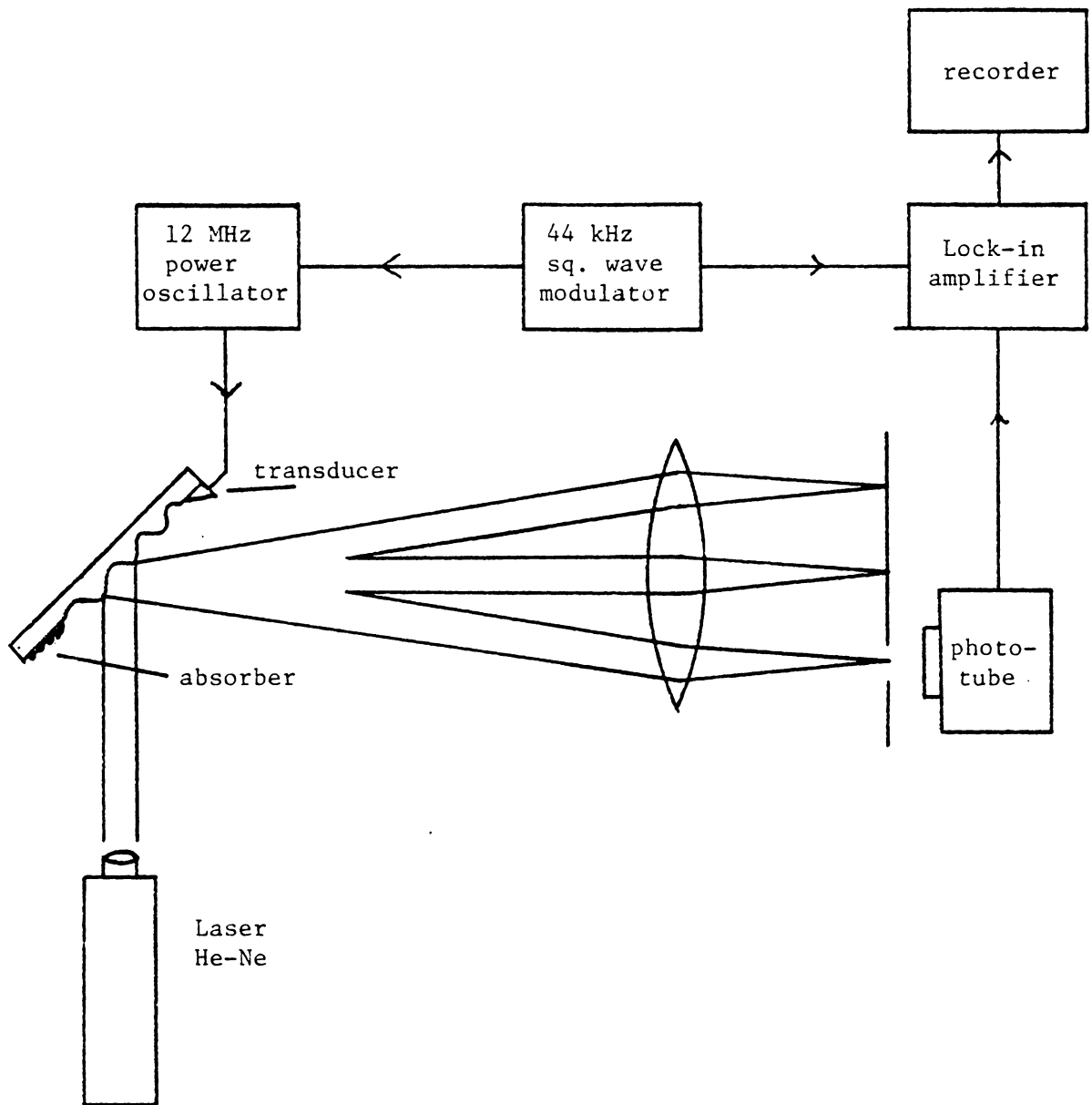


Figure 1.7. Experimental configuration for detection of surface waves by optical diffraction [12].

ency between 95 and 99% [5]. The higher the reflectivity, the more distinct the interference profile, however, the SAW sensitivity is reduced by the low output optical power.

Experimental configurations generally have one plate supporting propagating SAW. The transfer mechanism of the SAW to the plate can be achieved by fluid coupling between a source substrate and the interferometer plate as shown in Figure 1.8 or by generating the SAW directly onto the interferometer plate. Direct generation is convenient only for transparent materials such as glass lithium niobate and quartz. The propagating SAW modulates the separation distance between the interferometer plates. The resulting interference pattern modulates spatially, synchronous to the SAW frequency. The Fabry-Perot technique is capable of detecting SAW displacements of approximately  $10^{-7}$  Å [5]. Furthermore, frequency analysis can be performed by the Fabry-Perot interferometer with resolution of two megahertz to several gigahertz. This is achieved by the detection of upper order interference circles lying between the maxima in the principle interference pattern. The particular resolution is determined by the physical geometry of the parallel interferometer plates.

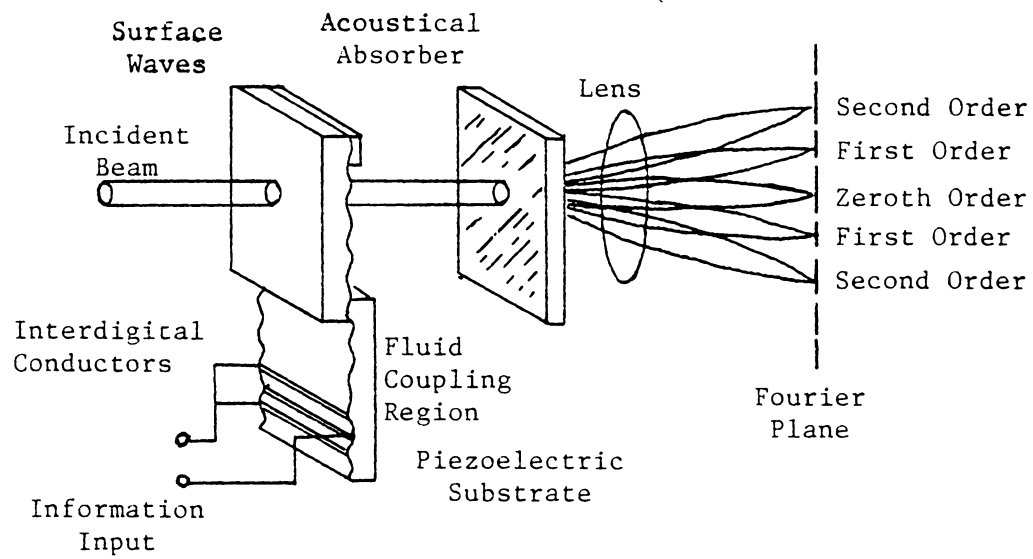


Figure 1.8. Surface wave detection using Fabry-Perot Interferometer [5].



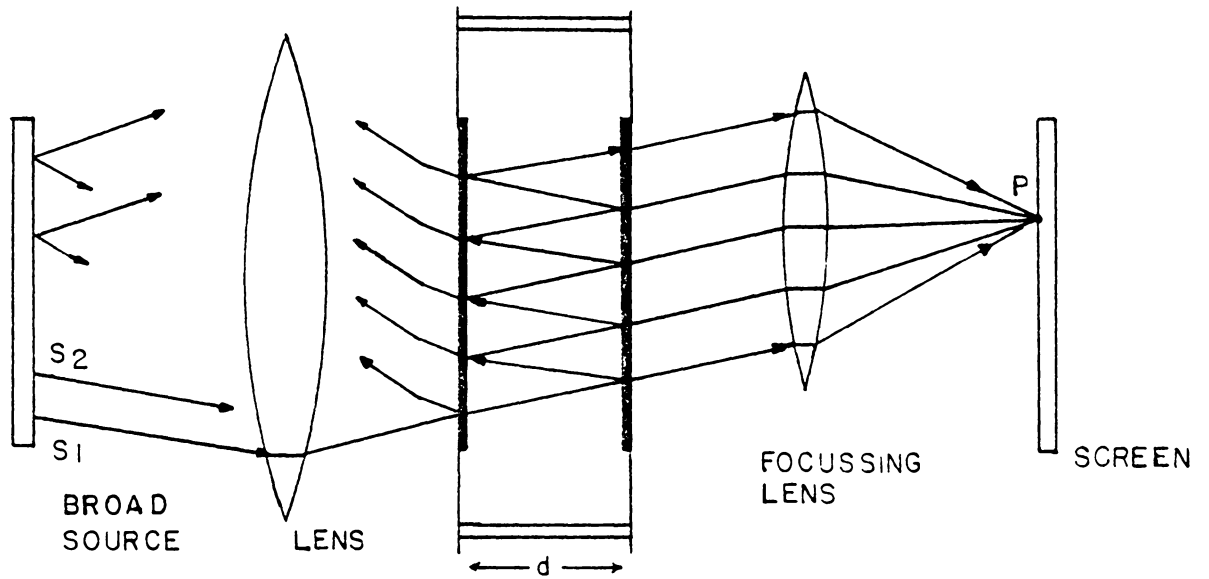


Figure 1.9. Light ray scatter in a Fabry-Perot Interferometer [13].

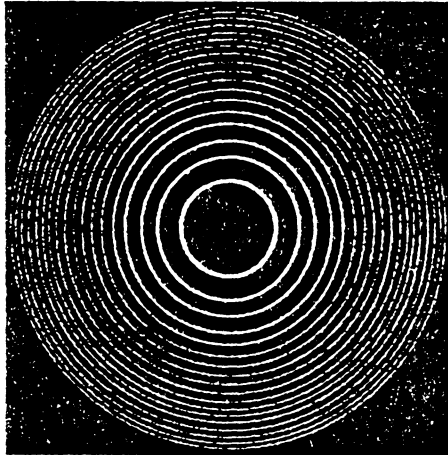


Figure 1.10. Interference pattern generated by a Fabry-Perot Interferometer [13].

Other interferometric techniques beat two optical beams to produce an interferometric intensity pattern which is spatially modulated. In one, a several wavelength broad optical beam is reflected off the specimen surface on which an acoustic surface wave is propagating. The incident beam is diffracted by the surface and in the near field the +1 or -1 orders beat with the zero order [5,11]. This interference pattern is spatially modulated due to the optical interaction with the periodic SAW. The modulated optical interference pattern, passed through a spatial filter matching the periodicity of the interference pattern, produces a signal at the detector of [5]

$$\int 2E_i^2 R^2 k_i \delta |\cos(\Omega t - kx)| dx, \quad (1.17)$$

where  $E_i$  is the incident optical field amplitude,  $R$  is the reflection coefficient,  $\delta$  is the SAW amplitude,  $k_i$  is the optical field wavenumber,  $\Omega$  is the SAW radian frequency and  $k$  is the SAW wavenumber. The integration is over the physical dimension of the spatial filter. Unfortunately, the use of the optical spatial filter limits the system to low frequencies of SAW.

The second system is a differential optical pathlength interferometer which uses two optical probes reflected

from the specimen to form an interference region. This is shown in Figure 1.11 [5,14,15]. The differential interferometer is shot-noise limited to minimum detectable SAW amplitudes on the order of  $10^{-30}$ . It has adjustable SAW frequency sensitivity or can be utilized as a broadband detector. In addition, the differential probing characteristic makes the system insensitive to low frequency acoustical noise and specimen vibration. Furthermore, signal feedback for system stability is not required. It is an effective system for lower frequency surface wave detection for use in laboratory conditions. This system is the subject of further analysis in Chapter 3.

### 1.3. REPORT OVERVIEW

The development of robust methods for the detection and analysis of SAW is of continuing importance due to increased interest in SAW application in nondestructive evaluation, materials evaluation and signal processing devices. In the section 1.2 a brief overview of optical SAW visualization techniques is given. Emphasis is placed on the system's structure and theoretical sensitivity. In practice, the theoretical sensitivity is rarely obtained due to the non-ideal presence of background acoustical

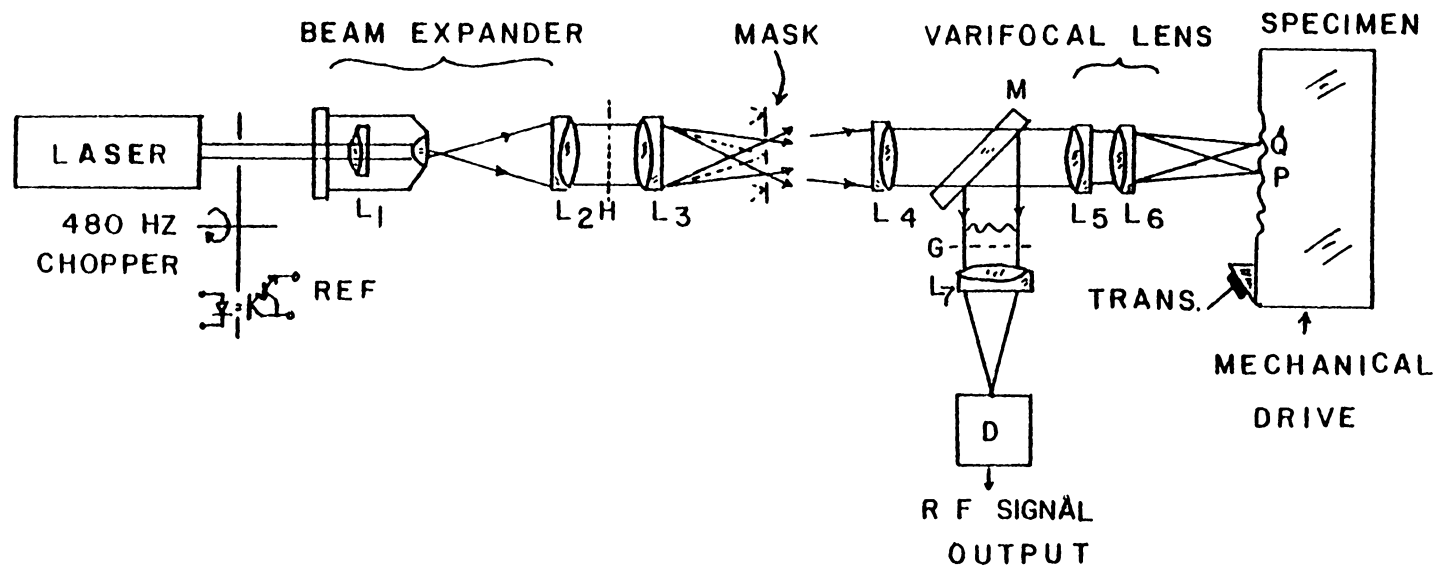


Figure 1.11. An experimental configuration for the two-beam differential interferometer [15].

noise, imperfect substrate surfaces (including low reflection coefficients), substrate motions and optical aberrations. The optical technique developed by Palmer, however, has the potential to reduce the degradation of system sensitivity due to occurrences of acoustical noise and surface irregularities. In the following chapters, a full description is given of the differential interferometer for SAW measurement reported by Palmer, Claus and Fick. One limitation of their system is noted and a new conceptualization of the differential interferometric technique is expanded and tested in experimentation.

## II. THEORETICAL DEVELOPMENT OF SURFACE ACOUSTIC WAVES

### 2.1. A MATHEMATICAL DESCRIPTION OF SURFACE ACOUSTIC WAVES

In a general framework, surface acoustic waves are a subclass of Rayleigh waves, named after Lord Rayleigh who first considered the phenomenon. Although surface waves were mathematically predicted during the last century by Rayleigh, the application of SAW in nondestructive evaluation did not evolve until basic theoretical considerations of wave propagation in the presence of material discontinuities were considered in the 1940's [16]. Many SAW testing techniques have been developed in the interim years for a wide variety of nondestructive evaluation applications, a few of which have previously been described in Section 1.2.

Rayleigh waves propagate along the plane boundary between an elastic half-space and a sufficiently rarified medium such as vacuum or air where the amplitude of the particle displacement caused by the wave motion decays as a function of depth into the half-space [5,16,17,18,19]. The mathematical description of the particle displacements can be solved by several methods, one of which is enumer-

ated below. All the solution methods are based on applying the appropriate boundary conditions to bulk body wave equations [16,17,19]. Their differences lie in the description of particle displacements, either by Newtonian momentum equations of motion or by potential functions of the stress field associated with the material deformation.

For this theoretical development of the propagation of Rayleigh waves, a consistent set of physical interpretations and variable definitions is necessary. Thus, a brief review of particle vector mechanics precedes the derivation and will lead naturally to the appropriate boundary conditions needed to generate the Rayleigh wave solution. To begin, consider two particles in an homogeneous medium of infinitesimal volume  $V$  and surface area  $S$ . The position of particle  $P_0$  is given by the vector  $\vec{x}$  from an arbitrary origin and the other particle,  $P_1$ , is located relative to  $P_0$  by vector  $d\vec{x}$  as seen in Figure 2.1 [17]. Deformation of the volume relocates  $P_0$  and  $P_1$  to  $P'_0$  and  $P'_1$ , respectively, with new position vectors  $\vec{x}'$  and  $d\vec{x}'$ .

Let  $\vec{u}$  be defined as the displacement vector of point  $P_0$  to  $P'_0$  so from Figure 2.1 it is determined that

$$\vec{u} = \vec{x}' - \vec{x}. \quad (2.1)$$



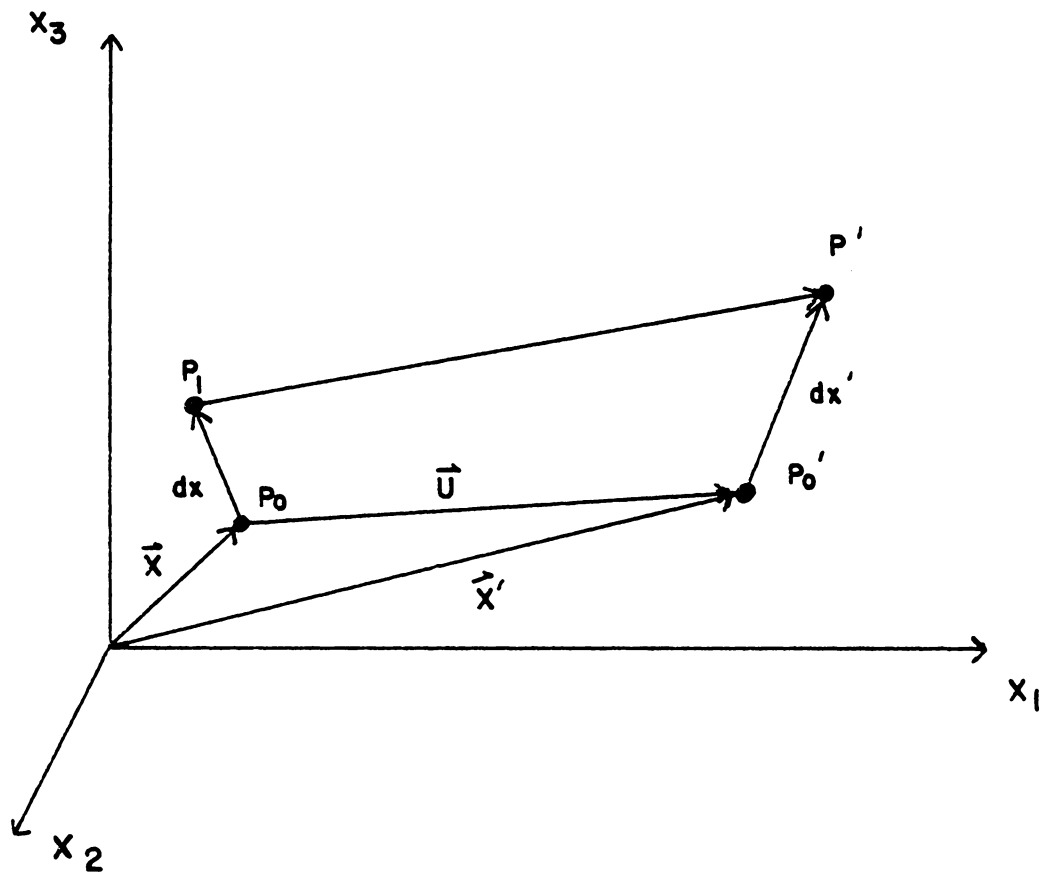


Figure 2.1. Differential particle displacement in a strained material [17].

Thus, the differential form of the particle displacement  $\vec{u}$  is

$$d\vec{u} = d\vec{x}' - d\vec{x} . \quad (2.2)$$

This is the differential particle displacement of the medium [17]. The linearized Taylor expansion of one component  $du_i$ ,  $i=1,2,3$ , can be written as

$$du_i = u_{i,j} dx_j , \quad (2.3)$$

following Einstein tensor notation.  $u_{i,j}$  represents the displacement gradient matrix  $\vec{E}(\vec{x},t)$  and is a measure of the differential displacement of particles in a deformed medium.  $\vec{E}(\vec{x},t)$  can be decomposed into symmetric and antisymmetric parts. The symmetric part is the measure of local material deformation, or the strain field  $\vec{S}(\vec{x},t)$ , and the antisymmetric differential displacement corresponds to local rigid-body rotation. Specifically, the strain field is [17]

$$S_{ij} = (1/2)(u_{i,j} + u_{j,i}) , \quad (2.5a)$$

and the rotational field is

$$R_{ij} = (1/2)(u_{i,j} - u_{j,i}) . \quad (2.5b)$$

Since we are interested in local deformation and not rigid-body motions, the strain field is of primary inter-

est for linearized particle displacement kinematics.  $S_{ij}$  describes the linear relation between displacement of particles in the  $i^{\text{th}}$  direction while moving in the  $j^{\text{th}}$  coordinate direction. A similar relationship is defined for traction forces on the surface of the volume [17,18]. Having the units of force per unit area, the stress field  $\vec{T}(\vec{x}, t)$  has components  $T_{ij}$  defined as the  $i^{\text{th}}$  component of force density acting on the  $j^{\text{th}}$  face of an infinitesimal volume. The traction force vector on the surface of a face perpendicular to the unit normal  $\hat{n}$  pointing out of the volume is defined as

$$\vec{T}_n(\vec{x}, t) = \vec{T}(\vec{x}, t) \cdot \hat{n} . \quad (2.6)$$

The integrated surface force acting on an infinitesimal volume is

$$\int_{\delta S} \vec{T} \cdot \hat{n} \, dS, \quad (2.7)$$

so that the application of Newton's third law gives

$$\int_{\delta S} \vec{T} \cdot \hat{n} \, dS = \int_{\delta V} \rho \frac{\partial^2 u}{\partial t^2} \, dV , \quad (2.8)$$

$$\nabla \cdot \vec{T} = \lim_{\delta V \rightarrow 0} \frac{\int_{\delta V} \vec{T} \cdot \hat{n} \, dS}{\delta V} , \quad (2.9)$$

Equation (2.8) becomes

$$\nabla \cdot \vec{T} = \rho \frac{\partial^2 u}{\partial t^2} , \quad (2.10)$$

the translational equation of motion for a vibrating medium. In indexed notation, Equation (2.9) is represented by [17,18]

$$\frac{\partial T_{ij}}{\partial x_j} = \rho \frac{\partial^2 u_i}{\partial t^2}, \quad (2.11)$$

Hooke's Law of vibrating bodies states that stress is linearly proportional to strain, or, in other words, that the amplitude of particle displacement is linearly related to the restoring forces. This relationship can be written as [17]

$$T_{ij} = c_{ijkl} S_{kl}, \quad (2.12a)$$

where the  $c_{ijkl}$  are the elastic stiffness constants. The inverse relationship [17],

$$S_{kl} = s_{klij} T_{ij}, \quad (2.12b)$$

has the linear relationship expressed in the compliance constants,  $s_{klij}$  which are small valued for rigid materials.

Boundary conditions can now be applied to the wave equation of the linear, homogeneous medium. Consider the semi-infinite half-space shown in Figure 2.2. The material boundaries are defined by  $-\infty \leq x_1 \leq \infty$ ,  $-\infty \leq x_2 \leq \infty$  and  $0 \leq x_3 \leq \infty$ . The boundary conditions which exist at the surface,  $x_3 = 0$ , are  $T_{31} = T_{32} = T_{33} = 0$ . Assuming

wave propagation in the  $\vec{x}_1$  direction with propagation vector  $\vec{k}_1$ , the solution to Equation (2.11) is the linear combination of partial waves of the form [19]

$$u_j = \alpha_j \exp(-ikb x_3) \exp(ik(x_1 - vt)), \quad (2.13)$$

where the phase velocity is  $v$  and the wave amplitude decays as  $x_3$  goes to infinity with decay constant  $kb$  [F]. These equations can be abbreviated by using the summation convention to write [17,18]

$$u_j = \alpha_j \exp(ik(b_i x_i - rt)), \quad (2.14)$$

where  $b_1 = 1$ ,  $b_2 = 0$ , and  $b_3 = -b$ . Each partial wave must satisfy the wave equation (2.11), which yields upon substitution,

$$(c_{ijkl} b_i b_j + \delta_{jk} v^2) = 0. \quad (2.15)$$

This is a sixth order operation in  $b$  with real coefficients for a specified value of  $v$  [19]. The roots  $b^{(n)}$  of (2.15) are real or occur in complex conjugate pairs [F]. Those lying on the real axis or in the lower half of the complex plane lead to non-vanishing wave amplitudes in the positive  $\vec{x}_3$  direction. Therefore, in general, there exist three roots which satisfy the wave equation and vanish with increasing distance along  $\vec{x}_3$ . The three resulting linearly independent partial wave equations with wave amplitude components

$\alpha_j^{(n)}$  are combined with appropriate weighting coefficients,  $C_n$ , to match boundary conditions.

The solution gives rise to a unique phase velocity. In the linear case,  $v$  is frequency independent. The decomposed particle displacement partial wave equations can now be written as

$$u_j = \sum_{n=1}^3 C_n \alpha_j^{(n)} \exp[ik(b_i^{(n)} x_i - vt)] , \quad (2.16)$$

where  $b_1^{(n)} = 1$ ,  $b_2^{(n)} = 0$ , and  $b_3^{(n)} = b^{(n)}$ . Solutions of the resulting eigenvalue problem where the  $b^{(n)}$ 's and  $\alpha_j^{(n)}$ 's are the eigenvalues and eigenvectors, respectively, are determined by solving the matrix equation

$$\det|r_{ij} - \delta_{ij} v^2| = 0 , \quad (2.17)$$

where  $r_{ij} = b_k b_i c_{kijl}$ . Equation (2.17) is an algebraic equation in  $b$  for given values of  $v$ . The Rayleigh velocities are solved for by substituting (2.14) into the boundary conditions

$$r_{3j} = C_{3jkl} \frac{\partial u_k}{\partial x_1} = 0 , \quad (2.18)$$

which yield,

$$c_{3jkl} k^{(n)} b_1^{(n)} C_n = 0. \quad (2.19)$$

This is an implicit equation in  $v$ ,

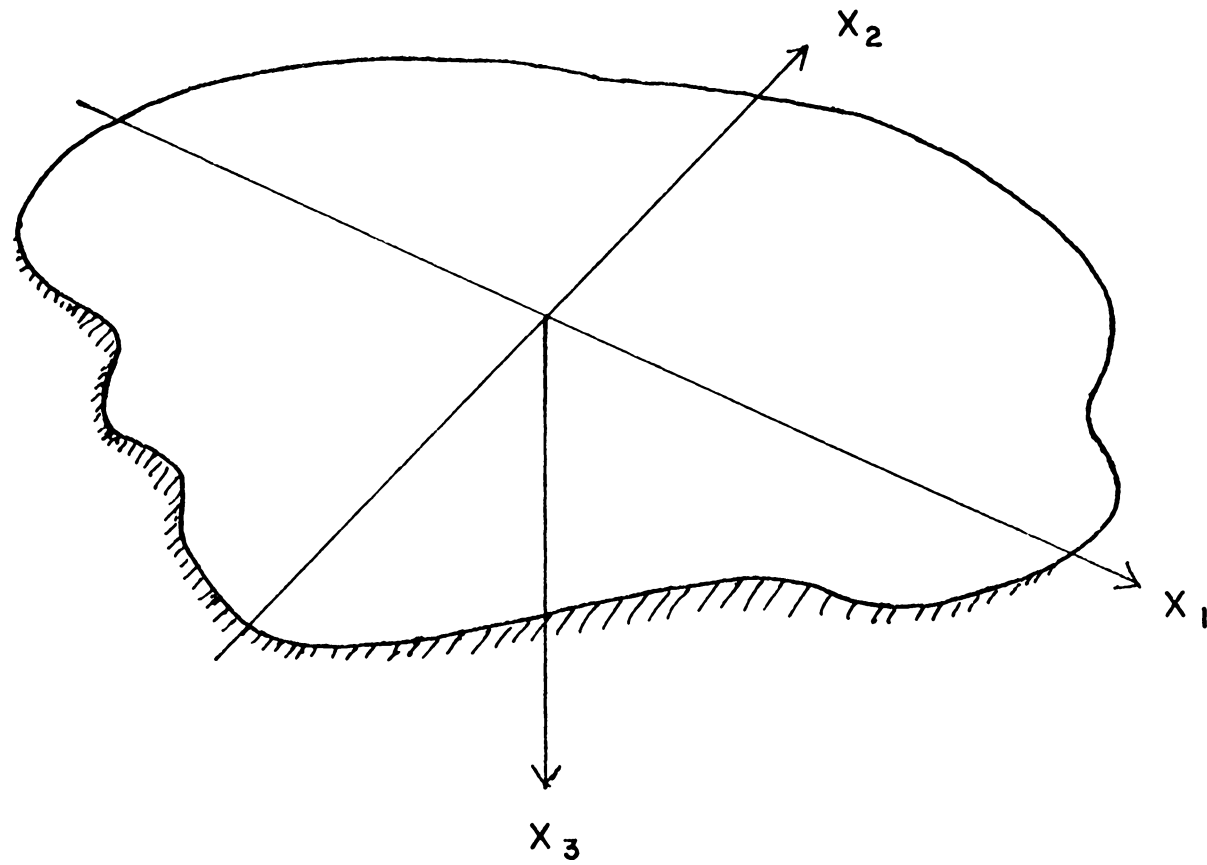


Figure 2.2. Half-space coordinate geometry.

$$\det |c_{3jkd} \alpha_k^{(n)} b_1^{(n)}| = 0, \quad (2.20)$$

which is generally necessary to solve by numerical methods. Arriving at a solution for  $v$ , (2.17) can now be used to determine the  $b^{(n)}$ 's and the  $\alpha_j^{(n)}$ 's.

For isotropic substrates, the elastic stiffness constants are reduced to two values,  $c_{11}$  and  $C_{44}$ , the Lamé constants. Furthermore, the symmetry conditions on the elastic constant tensor reduces the equations of (2.17) to the following set of equations [19]:

$$\begin{aligned} \Gamma_{11} &= C_{11} + C_{44}b^2 & \Gamma_{12} &= 0 & \Gamma_{13} &= (C_{11} - C_{44})b \\ \Gamma_{21} &= 0 & \Gamma_{22} &= C_{44}(1+b^2) & \Gamma_{23} &= 0 \\ \Gamma_{31} &= (C_{11} - C_{44})b & \Gamma_{32} &= 0 & \Gamma_{33} &= C_{44} + C_{22}b^2 \end{aligned} \quad (2.21)$$

Consideration of bulk waves in an infinite medium further reduces (2.17) since  $b = 0$  for the unbounded case. The longitudinal wave and two degenerate shear wave velocities can thus be determined to be [19]

$$v_\ell = \sqrt{c_{11}/\rho} \quad (2.22a)$$

and

$$v_t = \sqrt{c_{44}/\rho} \quad (2.22b)$$



where  $v_\ell$  is the longitudinal wave velocity and  $v_t$  is velocity for both shear waves.

The three solutions for eigenvalues  $b^{(n)}$  and associated eigenvectors  $\alpha_j^{(n)}$  can be decoupled into two wavemodes [18,19]. One solution corresponds to a bulk shear wave polarized perpendicularly to the sagittal plane of the desired surface wave. The other two solutions give rise to two wave components polarized in the sagittal plane and are the solution by components to the Rayleigh wave equation. Thus, solving (2.17) in consideration of (2.21) and substituting  $b^{(n)}$  and  $\alpha_j^{(n)}$  as functions of  $v$  into (2.19), the Rayleigh surface wave velocity  $v$  is found to be the solution to the implicit equation [16,17,18,19]

$$\left[ 2 - \left( \frac{v}{v_t} \right)^2 \right]^2 = 4 \left[ 1 - \left( \frac{v}{v_\ell} \right)^2 \right]^{1/2} \left[ 1 - \left( \frac{v}{v_t} \right)^2 \right]^{1/2}. \quad (2.23)$$

An approximate solution published by Viktorov with less than three percent error is [16]

$$\frac{v}{v_t} = \frac{0.72 - (v_t/v_\ell)^2}{0.75 - (v_t/v_\ell)^2}. \quad (2.24)$$

In isotropic media,  $v_t/v_\ell \leq 0.5$  and thus the Rayleigh velocity is seen to be bounded by  $0.87 < v/v_t < 0.96$  from

equation (2.24), approximately 90 percent of the shear bulk wave velocity [16,19].

The displacement components of the Rayleigh wave are given by [19]

$$u_1 = C[\exp(-kb_1x_3) - A \exp(-kb_2x_3)] \times \exp[ik(x_1-vt)] \quad (2.25a)$$

and

$$u_3 = +ikb_1C[\exp(-kb_1x_3) - A^{-1}\exp(-kb_2x_3)] \times \exp[ik(x_1-vt)] \quad (2.25b)$$

Here,  $b_1 = [1-(v/v_\ell)^2]^{1/2}$ ,  $b_2 = [1-(v/v_t)^2]^{1/2}$  and  $A = (b_1b_2)^{1/2}$ . All constants are positive, real quantities where the C's depend on the amplitude of the input excitation.

In units of relative amplitude and Rayleigh wavelength, Figure 2.3 plots the displacement components versus penetration depth generated by Equation (2.25) [16,18,19]. The resulting particle motion is seen as a retrograde elliptical displacement at the surface. The direction of revolution reverses in the interior of the body and both displacement components decay with depth into the mater-

ial. At two acoustic wavelengths beneath the surface, the amplitude of the displacement components has decreased by more than ninety five percent of that at the surface.

## 2.2. SURFACE WAVE GENERATION FROM BULK BODY ACOUSTIC EMISSION

Acoustic emission generates the three modes of bulk waves, namely, dilatational waves and two polarizations of shear waves. Two of these modes are shown in Figure 2.4 [17]. The conversion of these modes to surface displacements requires a complicated theory which must take into account possible preferred directions of propagation and AE sources which can selectively excite any mode or pair of modes [20]. For this discussion, the assumption will be made that all three modes are excited by an AE event and that these modes propagate with idealized spherical wavefronts without preferred directions. At the surface of the medium, the spherical wavefronts are incident as shown in Figure 2.5. In the surface area both inside and outside the angle  $\alpha_R$ , the surface displacement is due to the reflection of bulk waves off the surface. At the angle  $\alpha_R$ , however, the shear wave polarized in the z-direction has the projected wavelength of the Rayleigh wave at the

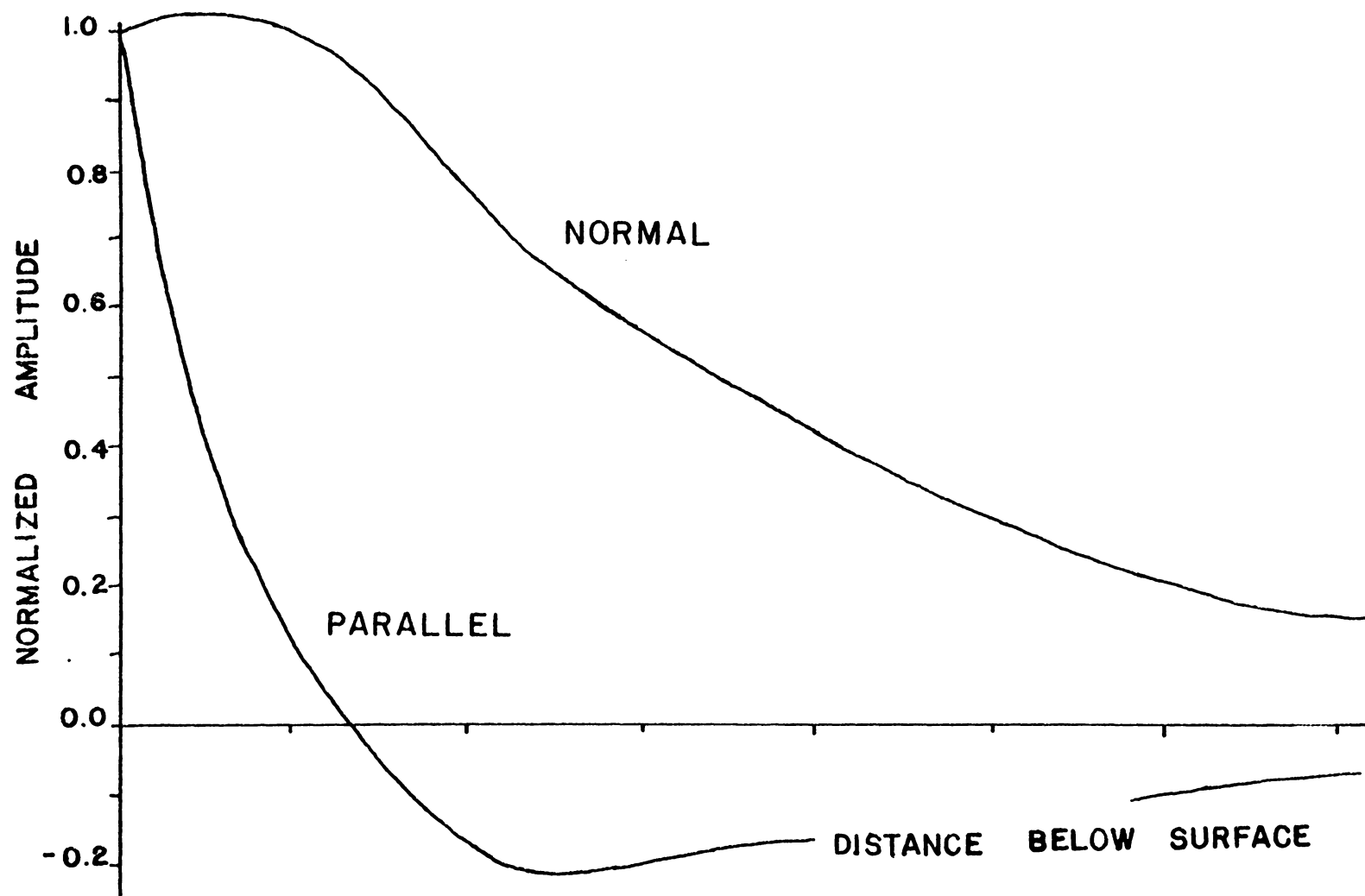


Figure 2.3. Theoretical SAW normal and parallel particle displacements to the direction of propagation as a function of depth.

surface. This excitation of the surface at the Rayleigh wavelength generates two Rayleigh waves, one propagating outward from the source center S and a weaker one propagating toward S. These Rayleigh waves are the SAW excitation fields used to characterize AE events.

Superimposed on this SAW are the surface displacements generated by the acoustic field of the AE incident on the remaining surface area. The frequency content of the AE event is broadband, so in general broadband detection is preferable. However, this imposes the problem of separating the acoustic surface wave from unwanted background acoustic field displacements. As discussed in the previous section, SAW travel with a slower velocity than either shear or longitudinal waves. In many cases, the longitudinal velocity is twice the shear velocity and Rayleigh wave velocities are approximately ninety percent of the shear. Thus, the acoustic surface displacement will be first impacted by the longitudinal wave, followed by the shear and then the Rayleigh wave. If the duration of the AE is appropriately short, then the signals may be resolved sufficiently for accurate detection.

The mode conversion from bulk to surface waves will be approximated by plane wavefronts for the spherically radiating AE. By writing the bulk wave equations and applying

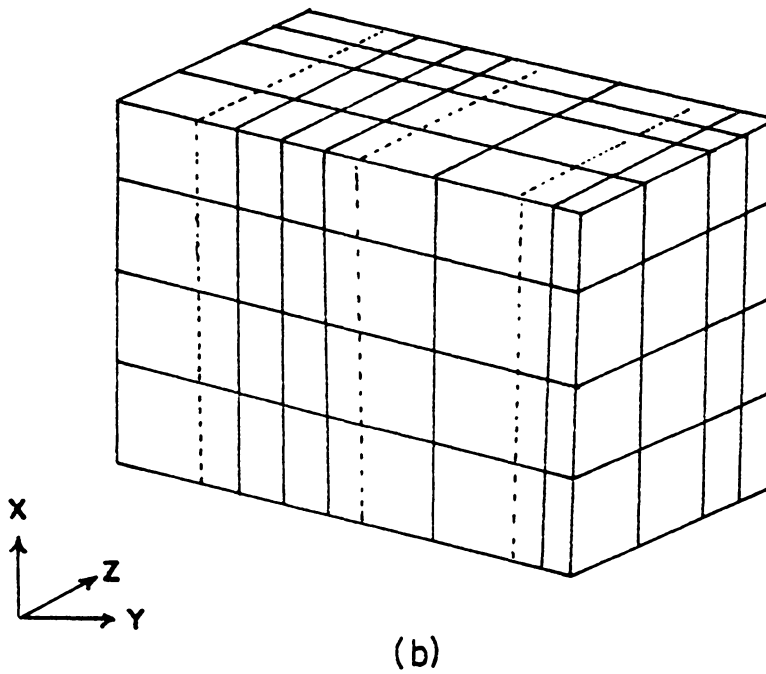
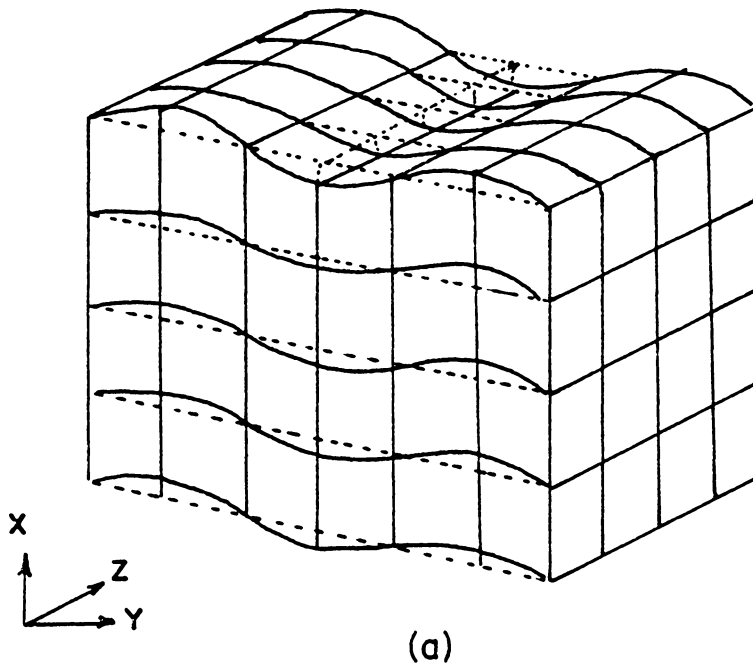


Figure 2.4. Two modes of y-direction acoustic propagation are (a) the x-polarized (shear) wave and (b) the y-polarized (compressional) wave. A third z-polarized wave is not shown. [17].

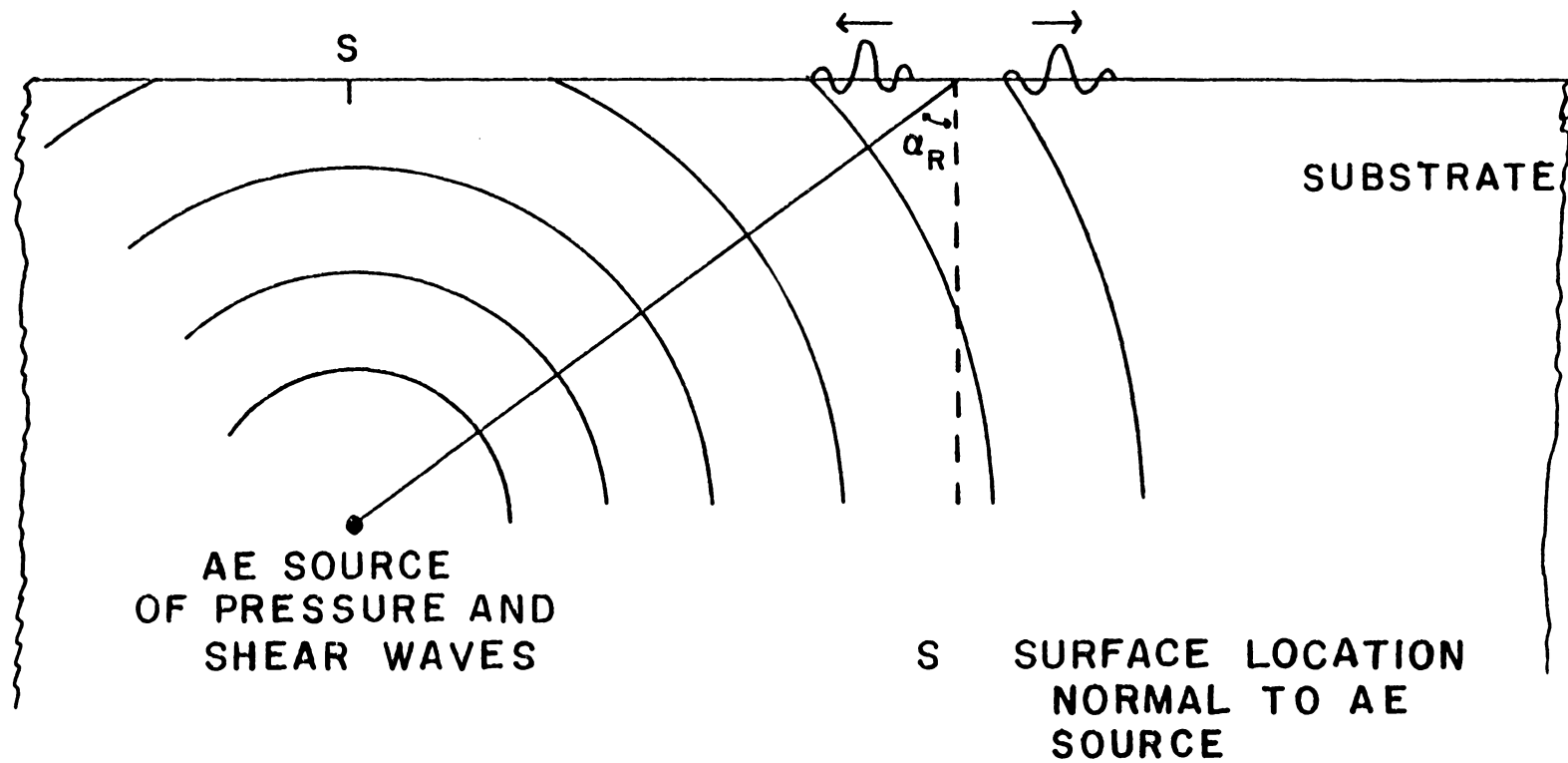


Figure 2.5. Bulk body acoustic emission couples to a surface wave.

the appropriate boundary conditions at the surface,  $T_{xx} = T_{xy} = T_{yz} = 0$ , the reflected bulk wave, including both dilatational and shear waves, can be expressed in a form of Snell's law applied to elastic media [21]. Specifically, the relationship between incident and reflected fields is given by

$$\frac{\sin \theta_1}{\sin \theta_2} = \frac{v_2}{v_1} = k \quad (2.26)$$

where  $\theta_1$  and  $\theta_2$  are the angles between  $\hat{y}$  and the pressure and shear wave normals, respectively, and

$v_1$  and  $v_2$  are their respective wavenumbers as shown in Figure 2.6. It has been shown that the  $\hat{y}$  polarized shear wave excites surface waves for incident angles greater than the critical angle  $\alpha_R$ . At the critical angle, a compressional plane wave propagating parallel to the surface and decaying in amplitude with depth into the medium is generated as shown in Figure 2.7.

### 2.3. USE OF SURFACE WAVES IN BOND EVALUATION

As an illustrative example of surface waves used in nondestructive evaluation, consider the experimental evaluation of the polymer adhesive bond between two metals in intimate contact. The strength of the bond is dependent on the strength of the polymer cross-bonding to the metal



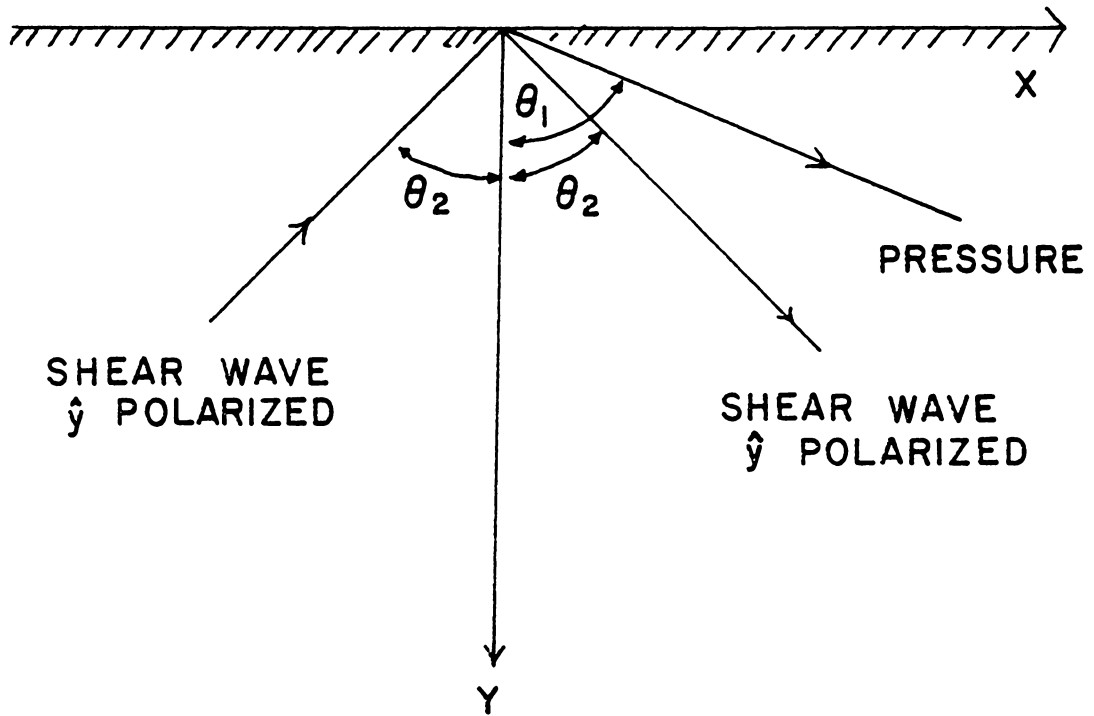


Figure 2.6. Decomposition of a surface reflected shear wave.

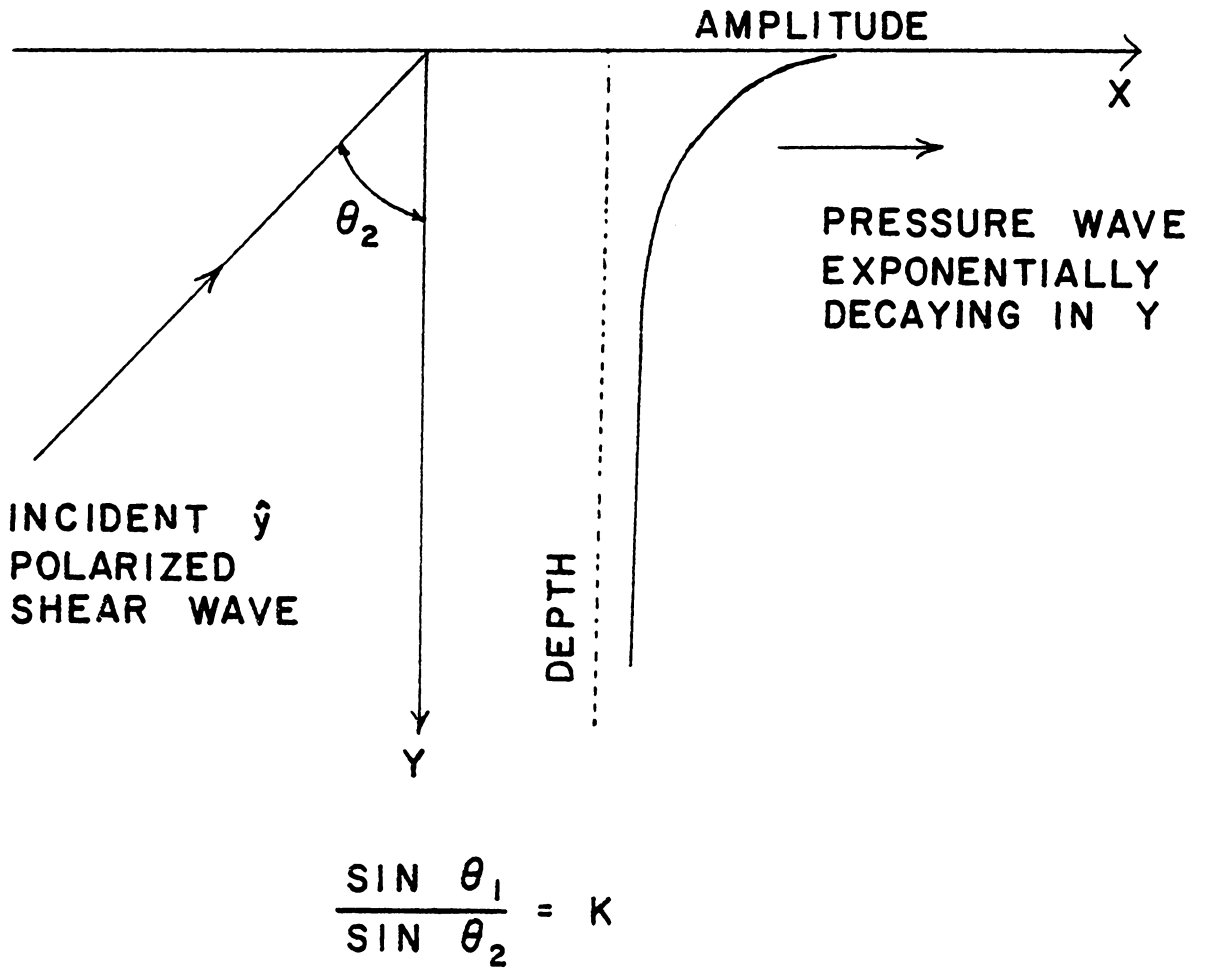


Figure 2.7. Decomposition of a surface reflected shear wave into a surface coupled pressure wave.

surfaces. Thus, the greater the incidence of cross-bonding, the stronger the bond. Of course, the physical conditions of the metal surfaces affect the bonding properties of the polymer as well so the surfaces are prepared prior to joining. There are no reported techniques for general inspection of the bonding surfaces which insure bond strength after curing, prior to the actual joining of the metals. Thus to insure adequate joint strength, inspection after bonding of the metals is required. Ultrasonic techniques hold great promise for this boundary layer analysis in determination of bond integrity of this type.

The parameters of a boundary between two bonded layers include adhesive layer thickness, debonding and delamination, voids, and stress versus time-in-use. In one simplified experiment, the detection of gross voids in the proximity of the boundary layer was measured [22]. In this experiment, a titanium bar 1.25 centimeters wide by 1 centimeter thick was bonded to an aluminum bar 10 centimeters wide by 7.5 centimeters thick as shown in Figure 2.8. The particular polymer adhesive and stress history of the experimental bar was unknown. However, the change of amplitude of ultrasonic waves transmitted through the boundary was less than 1dB while moving along the titanium

bar. This is depicted in Figure 2.8. Pulsed boundary waves were induced by propagating a surface wave generated by a wedge transducer into the boundary. The incident surface wave at the titanium boundary partially converted into Stoneley waves which propagate along the two metal boundary. Upon incidence at the receiver side's titanium-air boundary, the Stoneley wave partially reconverts to a surface wave propagating toward the receiver, also a wedge transducer.

Stoneley waves are the extension of Rayleigh waves to waves propagating along the boundary of two media [18]. In the limit of one medium going to a stress free region, such as air or vacuum, the Stoneley wave takes the form of a Rayleigh wave. At each point of mode conversion from Rayleigh waves to Stoneley waves and vice versa, bulk waves are excited and account for energy loss not measured in the transmitted and reflected waves along either the surface or the metal to metal boundary. To reduce the possibility of interference from the induced bulk waves, the propagation time of the pulsed signal was calculated and received signals were compared to this time for source verification.

To determine the effect of surface defects on Stoneley wave propagation [22], a clear-drilled hole shown in Fig-

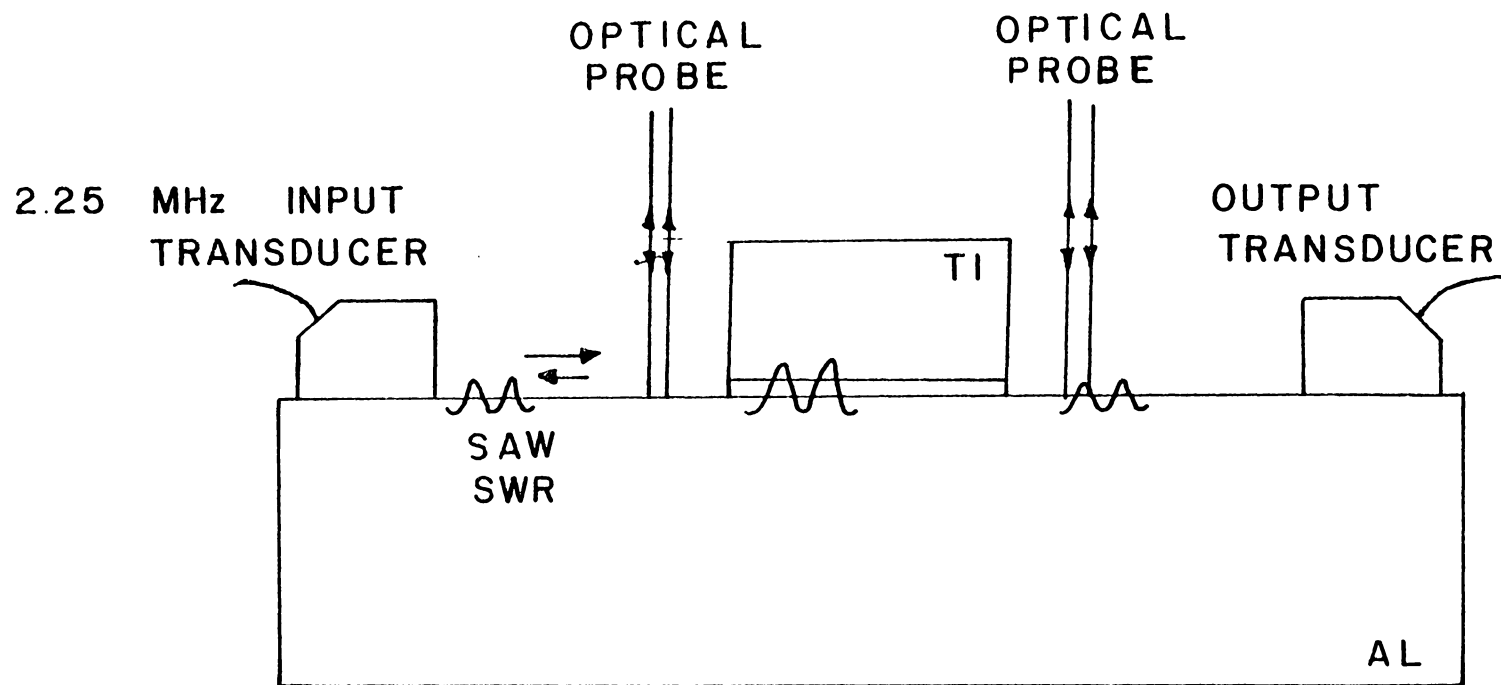


Figure 2.8. Experimental configuration for Al-Ti boundary layer evaluation [22].

ure 2.9 was made through the titanium and the aluminum to form a gross irregularity at the boundary. The source and receiver transducers were moved along the titanium bar past the irregularity and transmitted amplitude measurements were taken every five millimeters. The results of these measurement are shown in Figure 2.10a. In a second experiment the source transducer, as shown in Figure 2.8, was used to detect the reflected signal in pulse-echo configuration. Again the transducer was moved along the titanium face past the defect with the results shown in Figure 2.10b. Lastly, pitch-catch measurements of the wave amplitude were made at the location of a flat bottomed hole drilled in increments of 1 millimeter through the titanium into the aluminum. The results are given in Figure 2.11. The attenuation of the signal amplitude is seen in Figure 2.12 to increase as the boundary of the bottom of the hole approaches the aluminum-titanium interface. The rate of change of the attenuation with penetration is higher in the titanium than in the aluminum which supports the conclusion that energy propagates in disproportionate levels within the two metals along the boundary. In this case, results indicate that more energy is propagated in the titanium.

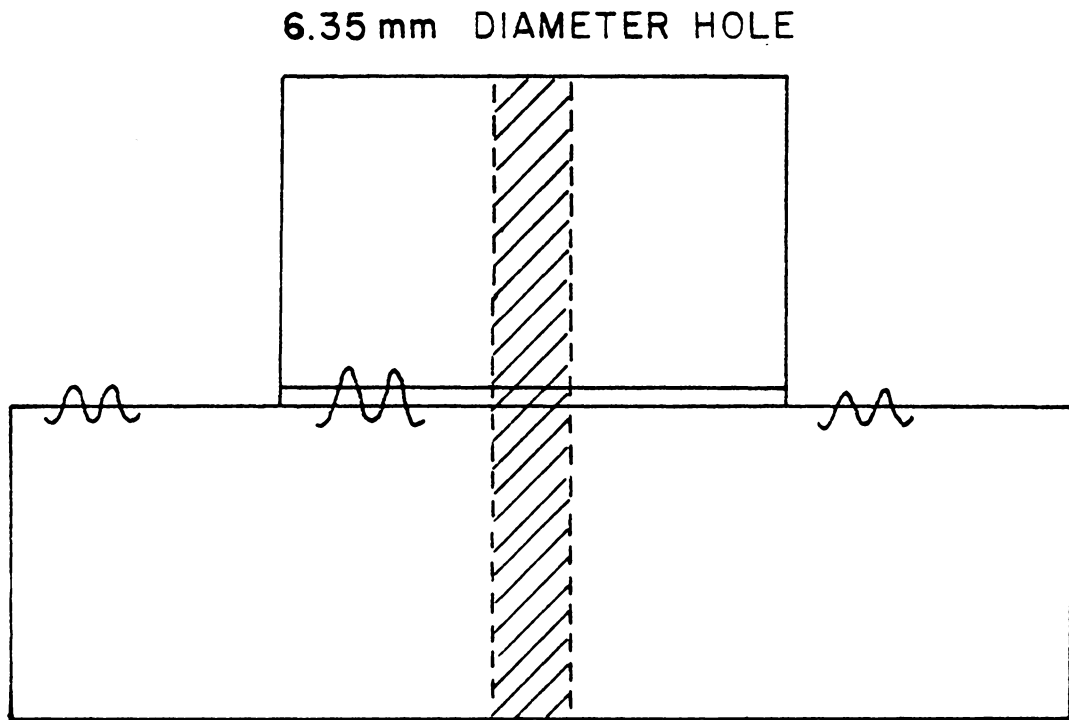


Figure 2.9. Clear drilled hole through Al-Ti boundary for measurement of Stoneley wave reflection and attenuation [22].

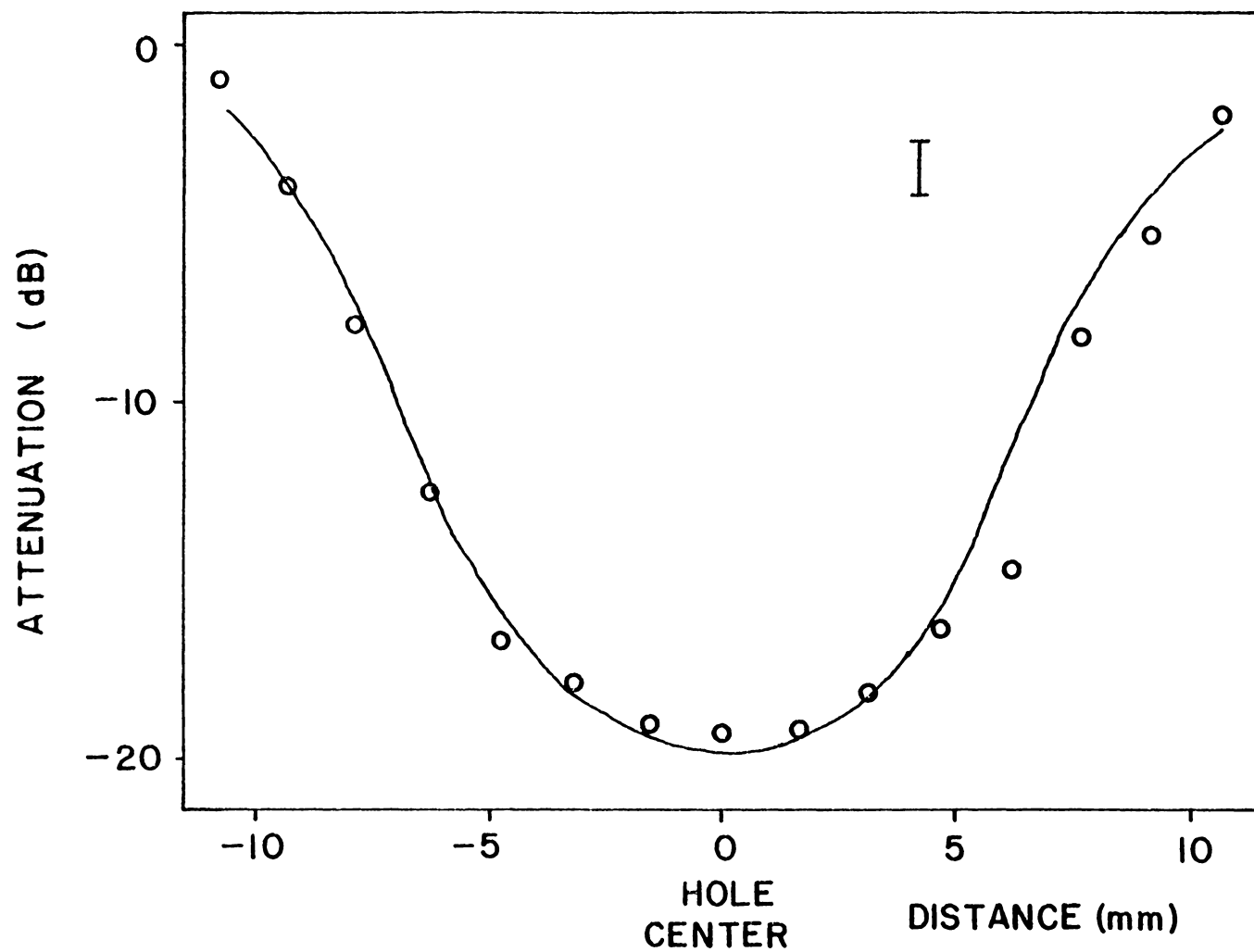


Figure 2.10a. Pitch-catch attenuation as a function of position along Al-Ti boundary [22].



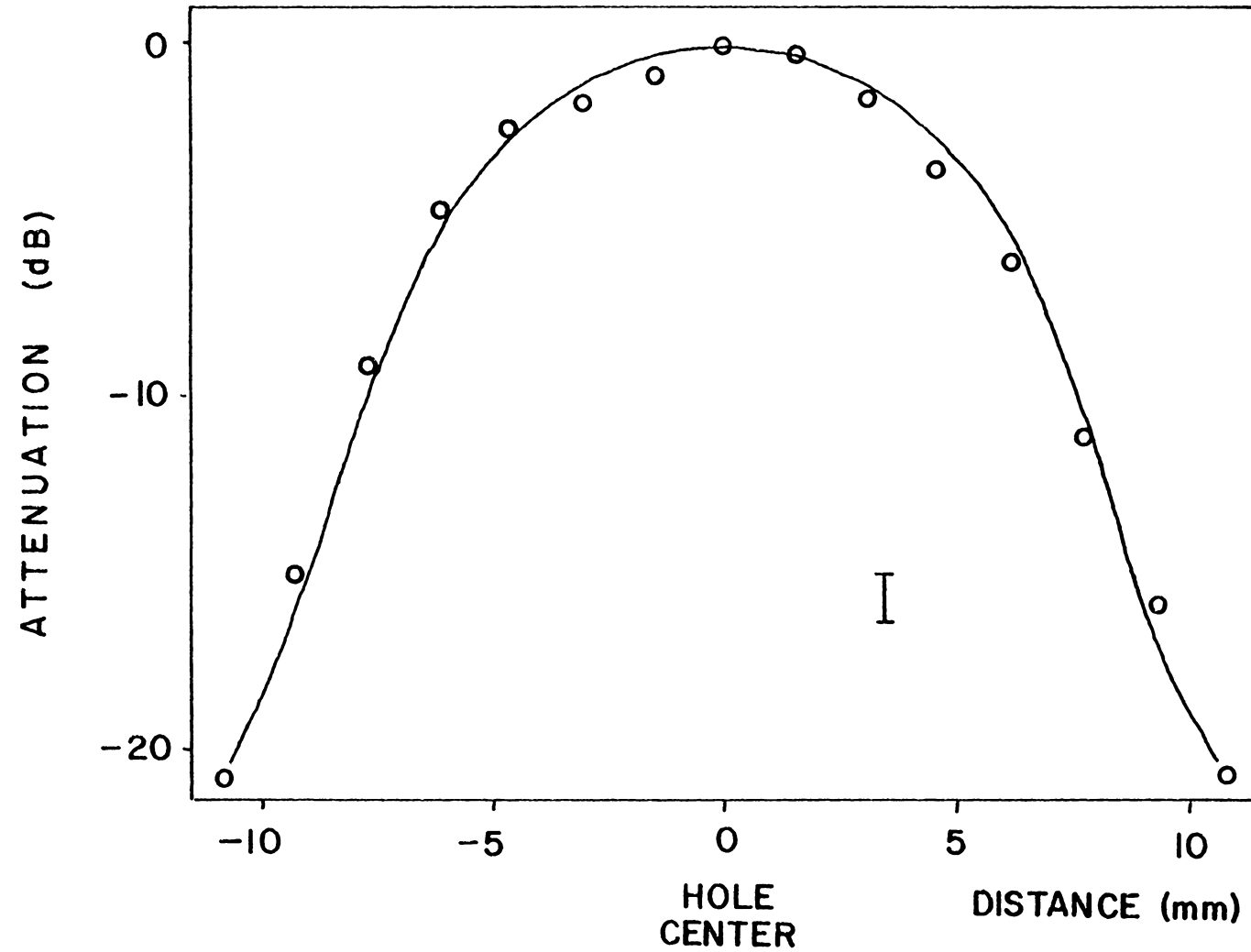


Figure 2.10b. Pulse-echo attenuation as a function of position along Al-Ti boundary [22].

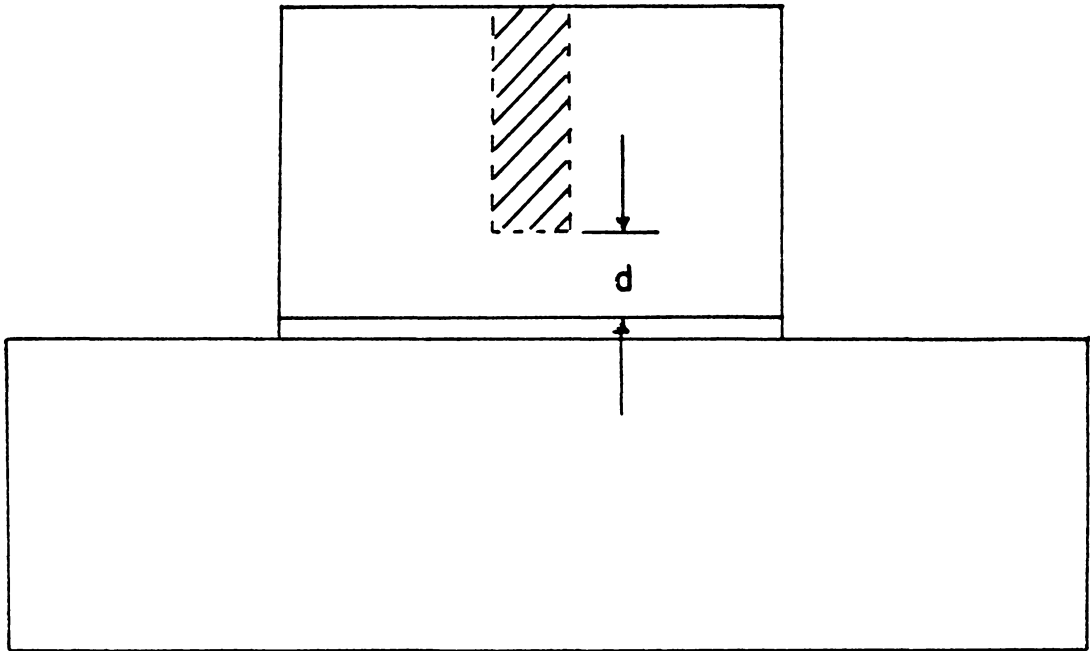


Figure 2.11. Square profiled clear drilled hole of decreasing distance from Al-Ti boundary. [22].

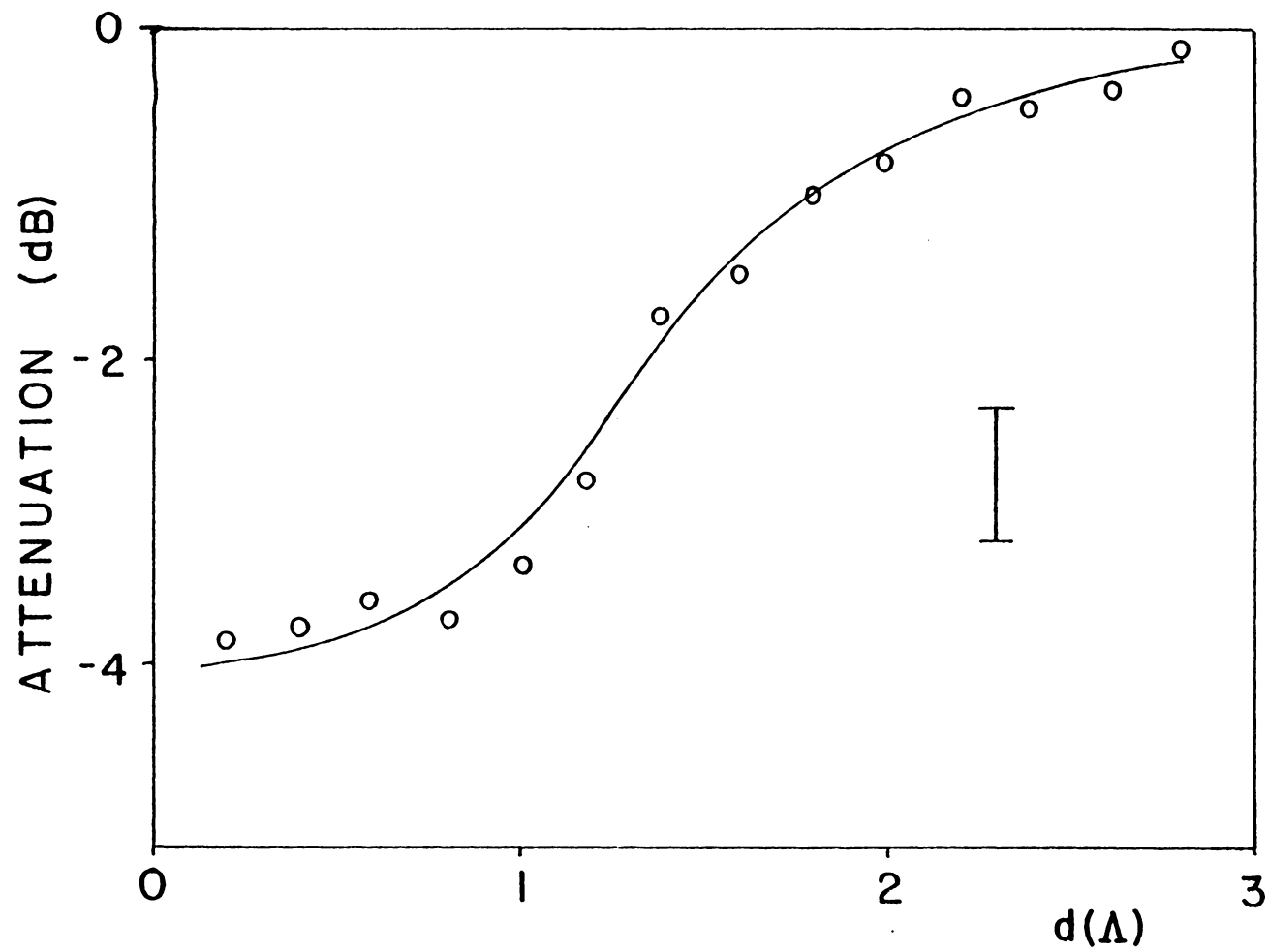


Figure 2.12. Pitch-catch attenuation as a function of defect distance from Al-Ti bond boundary [22].

In this experiment, it is shown that investigation of contact boundaries between two opaque materials can be implemented with the use of SAW techniques. SAW applications to the measurement of finer physical boundary properties will, of course, require more research. In this research, optical systems could be fully utilized for point resolution of transmitted and reflected fields. Furthermore, optical systems such as Adler's optical SAW scanner [9] or Palmer's differential interferometer [14,15] could permit differentiation among the propagation directions of waves in scattering analysis at boundary defects.

### III. THE DIFFERENTIAL INTERFEROMETER

#### 3.1. DEVELOPMENT OF THE DIFFERENTIAL INTERFEROMETER CONCEPTS

The differential interferometric technique utilized by Palmer, Claus and Fick offers significant advantages over other optical techniques as well as PZT contact transducers. Advantages of the interferometer include [15] 1) proportional signal output to optical path length changes, providing both SAW amplitude and phase information, 2) point-by-point vertical surface displacement measurements, 3) insensitivity to surface misalignments, irregularities and probe beam misfocus, and 4) easy calibration while maintaining an equal or superior sensitivity to other techniques. Following Palmer's notation [15], two coherent, collimated optical beams propagating at angles  $\pm\theta$  with respect to the surface normal, as shown in Figure 3.1, can be represented by

$$E_1 = E_0 \exp\{w_0 t - k[x \sin \theta + z \cos \theta] - \phi\}$$

and

$$E_2 = E_0 \exp\{w_0 t - \cancel{k}^k[-x \sin \theta + z \cos \theta] + \phi\}.$$

(3.1)

The constants  $E_0$ ,  $w_0$ , and  $k$  are, respectively, the field amplitude, radian frequency and wavenumber, and  $\phi$  is half the phase difference between the two waves. These representations can be generalized to a pair of collimated beams incident at angle  $\theta$  to the surface normal shown in Figure 3.2, which more accurately represents the experimental system. By performing a coordinate axis rotation in the positive direction with respect to the x-axis, the instantaneous field equations transform into

$$E_1 = E_0 \exp\{w_0 t - k[x \sin \theta - y \sin \theta \cos \theta + z \cos \theta] - \phi\},$$

(3.2)

and

$$E_2 = E_0 \exp\{w_0 t - k[-x \sin \theta - y \sin \theta \cos \theta + z \cos \theta] + \phi\}.$$

If properly aligned, the incident beams will reflect and overlap while propagating away from the surface. In this region of overlap, the combined field will have an amplitude given by

$$\begin{aligned} E &= E_1 + E_2 \\ &= 2E_0 \exp\{w_0 t - k(-y \sin \theta \cos \theta + z \cos \theta)\} \\ &\quad \times \cos(kx \sin \theta + \phi). \end{aligned}$$

(3.3)

The optical irradiance,  $H = E \cdot E$ , is then

$$H = 4E_0^2 \cos^2(kx \sin \theta + \phi).$$

(3.4)

By assuming a small relative propagation angle  $\theta$  between the two beams, the approximation  $\sin\theta \approx \theta$  can be used, giving [15]

$$H = 4E_0^2 \cos^2(kx\theta + \phi) . \quad (3.5)$$

Now taking the derivative of  $H$  and solving for the positions of optical intensity maxima and minima, they are found to be

$$x_{\max} = (n\pi - \phi)/k\theta , \quad (3.6)$$

and

$$x_{\min} = \left( \frac{\pi(2n-1)}{2} - \phi \right) / k\theta , \quad (3.7)$$

where  $n = \{0, 1, 2, \dots\}$  .

The intensity pattern described in (3.5) is a set of straight line interference fringes with fringe spacing [15]

$$\begin{aligned} x &= x_{a+1} - x_a = ((a+1)\pi - a\pi) / k\theta \\ &= \pi / k\theta \\ &= \lambda / 2\theta , \end{aligned} \quad (3.8)$$

where  $\lambda$  is the optical wavelength.

From the above discussion it is apparent that the interference fringes can be linearly displaced by a change

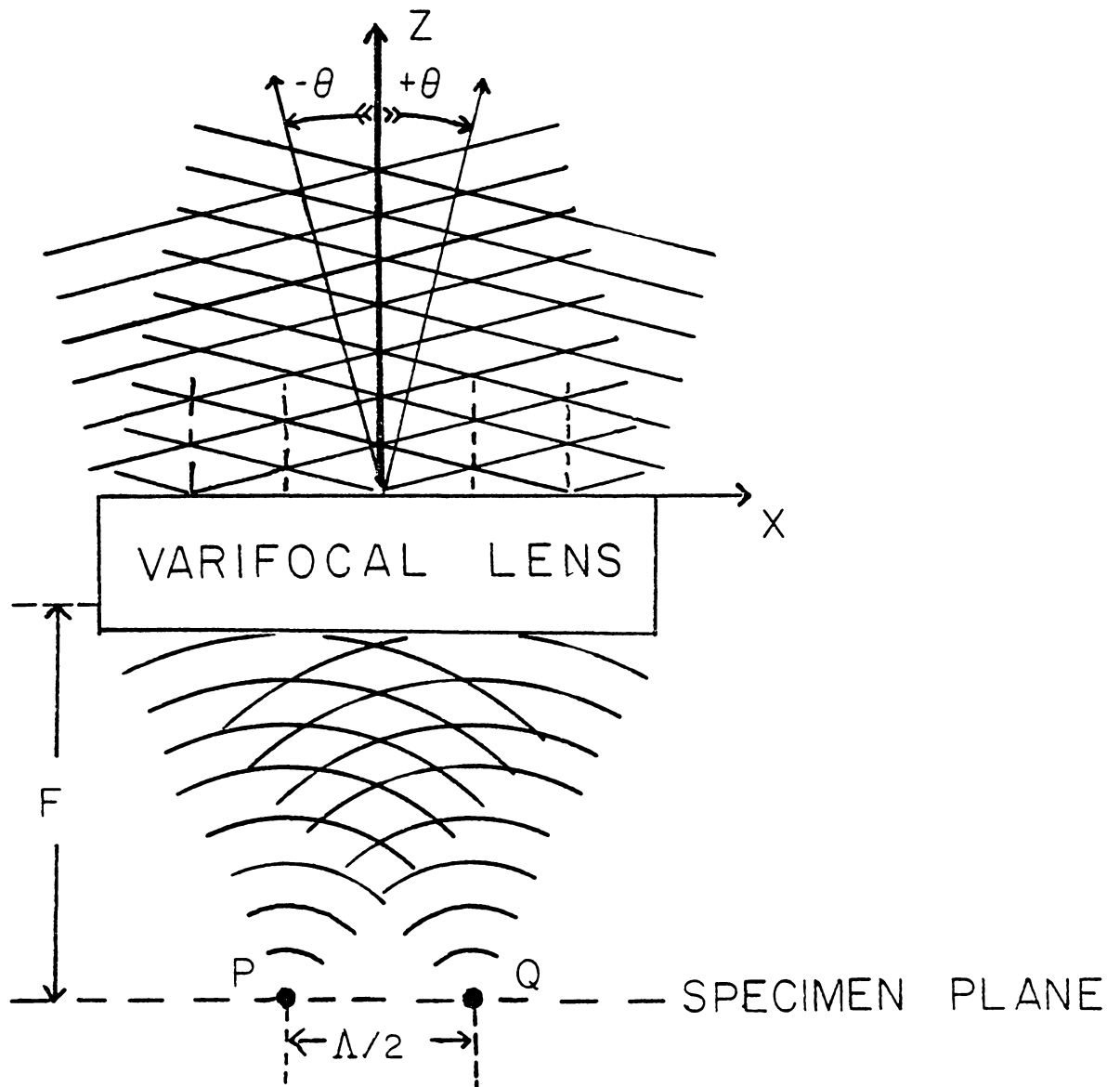


Figure 3.1. Dual beam geometry for the differential interferometer.



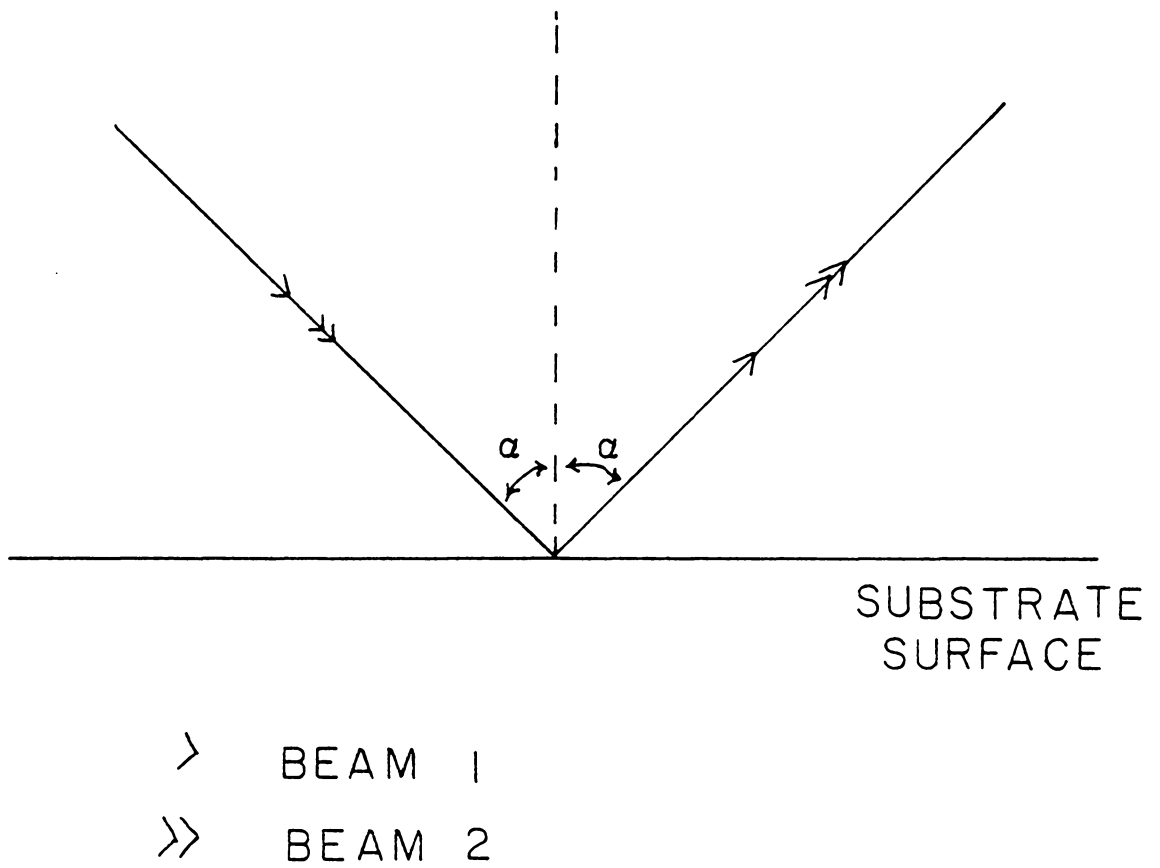


Figure 3.2. Incident angle of dual beams on specimen surface.

in  $\phi$  and remain undistorted in spacing. Thus, a Ronchi grid (square wave grating) with line spacing  $d = \lambda/2\theta$  can be inserted into the interference region to spatially demodulate light transmitted as the fringes translate in  $x$ . To determine an expression for the light transmitted by the entire grid, the light transmitted by a single slit may first be calculated as

$$\begin{aligned}\phi_1 &= \int_{x_1}^{x_1+d/2} H(x) dx \\ &= \int_{x_1}^{x_1+d/2} 4E_o^2 \cos^2(kx\theta + \phi) dx, \quad (3.9)\end{aligned}$$

where  $x_1$  defines the position of  $x$  at the front edge of one slit and  $x_1+d/2$  defines the following edge of the slit. Integrating (3.9), the light flux per slit is found to be [15]

$$\begin{aligned}\phi_1 &= E_o^2 d + \frac{-2E_o^2}{k\theta} [\cos(2k\theta x_1 + k\theta d/2 + 2\phi) \sin(\frac{k\theta d}{2})] \\ &= E_o^2 d - (2E_o^2 d/\pi) [\sin(2\pi x_1/d + 2\phi)], \quad (3.10)\end{aligned}$$

where the relations

$$\frac{k\theta d}{2} = \frac{\pi}{2} \quad (3.11)$$

and

$$2k\theta = \frac{2\pi}{d} \quad (3.12)$$

have been used. The total flux  $\Phi$  for  $m$  slits is then  $\Phi = m\Phi_1$ .

Now assume that the two collimated beams are focused on the surface by a varifocal lens. If the surface is traversed by an acoustic surface wave (see Figure 3.5), maximum pathlength modulation of the focused beams will occur when the optical focus spot separation is half the acoustical wavelength. Upon reflection from the surface, the optical beams can be recollimated by a similar varifocal lens producing the region of interference previously described. As shown in Figure 3.1, the separation of the focus points is related to the angle  $\theta$  by [15]

$$(\Lambda/2)/F = 2\theta \text{ (for small } \theta \text{)}, \quad (3.13)$$

and thus the lens focal length  $F$  is equal to

$$\begin{aligned} F &= \Lambda/4\theta \\ &= d\Lambda/2\lambda. \end{aligned} \quad (3.14)$$

By the proportional relation between the acoustic wavelength and the lens focal length, the focus spot point separation can be easily matched to  $\Lambda/2$ . Finally, noting that

$$\Phi = \overset{k}{(2\pi/\lambda)}\Delta L, \quad (3.15)$$

where  $\Delta L$  is half the optical pathlength difference, Equation (3.10) can be written as

$$\Phi/m = E_o^2 d - (2E_o^2 d/\pi) \sin[(2\pi x_1/d) + (4\pi/\lambda)\Delta L].$$

(3.16)

By modulation of  $\Delta L$ , the transmitted optical flux varies according to Equation (3.16), so that equation (3.16) can be linearized by making the assumption that  $\Delta L$  is much less than  $\frac{2}{\lambda}$ , the usual case. Equation (3.16) can then be written as

$$\phi/m = E_o^2 d - E_o^2 d (8\Delta L/\lambda) \quad (3.17)$$

where the arbitrary phase constant  $2\pi x_1/d$  is allowed to equal zero and the approximation

$$\sin[4\pi/\lambda \Delta L] = 4\pi/\lambda \Delta L \quad (3.18)$$

is made.

Equation (3.17) characterizes the linear relation between the transmitted flux and the pathlength difference  $2\Delta L$ .  $E_o^2 d$  is the constant flux component transmitted through the Ronchi grid and the modulated signal is contained in the second, modulated term. Summation of Equation (3.17) over  $m$  slits yields [15]

$$\phi = mE_o^2 d - mE_o^2 d (8\Delta L/\lambda) , \quad (3.19)$$

where the term  $E_o^2 d$  is recognized to have the units of power per unit distance. Assuming the Ronchi ruling to be sufficiently large to filter all incident light,  $mE_o^2 d$  would be proportional to half the incident optical power,  $P_o/2$ , where  $P_o$  is assumed to be the laser power incident

on the Ronchi grid. The total transmitted power which can be focused onto an optical detector will then be [15]

$$\begin{aligned} P &= P_O/2 - P_O/2(8\Delta L/\lambda) \\ &= P_O/2 - P_O(4\Delta L/\lambda) . \end{aligned} \quad (3.20)$$

The interference pattern due to the reflected beams is intensity demodulated when imaged on the Ronchi ruling. Assuming each fringe width to be perfectly matched to the width of the Ronchi ruling line, the transmission intensity versus the position of the fringe along the grid can be computed. The results of this computation are shown in Figure 3.3a. Greatest sensitivity for minute modulated shifts in the fringes is obtained at the inflection point of the graph. At this point, the change in transmitted intensity versus fringe translation across the Ronchi grid is maximized. The location on the grid of this maximum is at a one quarter fringe width shift from the superimposed position as shown in Figure 3.3b. The gain in using the Ronchi ruling to spatially filter the modulated fringes is two as compared to imaging a fringe directly onto the photodiode. Also, the intensity modulation as opposed to detection of a fringe shift allows the utilization of all available light.

An acoustic wave traversing the specimen surface with wavelength  $\Lambda$  would produce a time varying normal surface displacement with amplitude

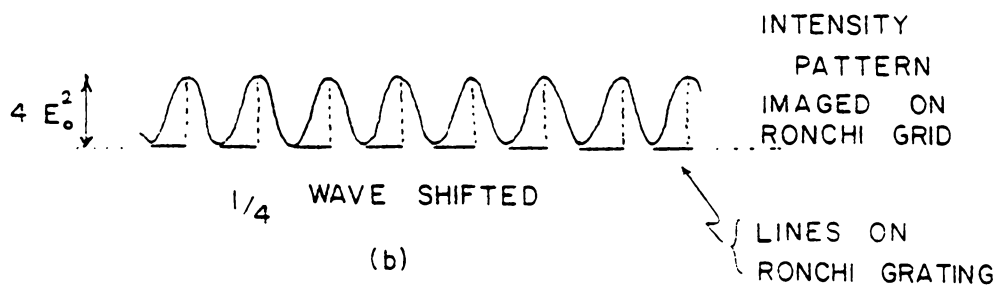
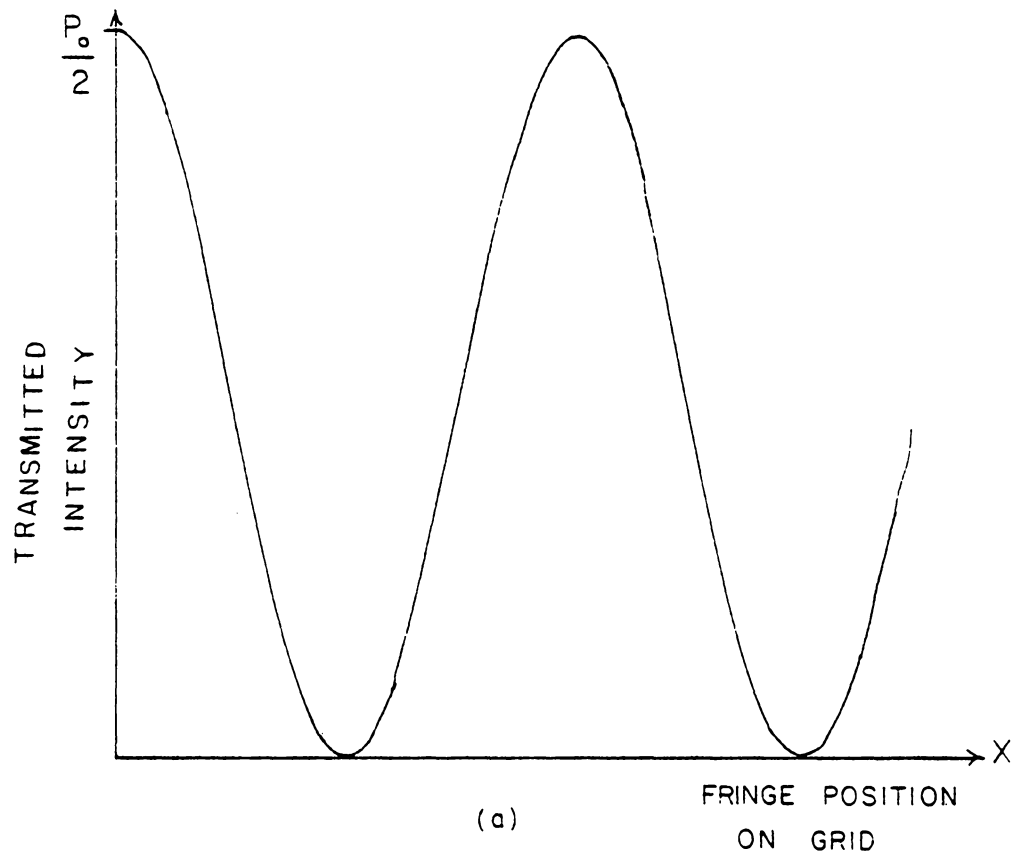
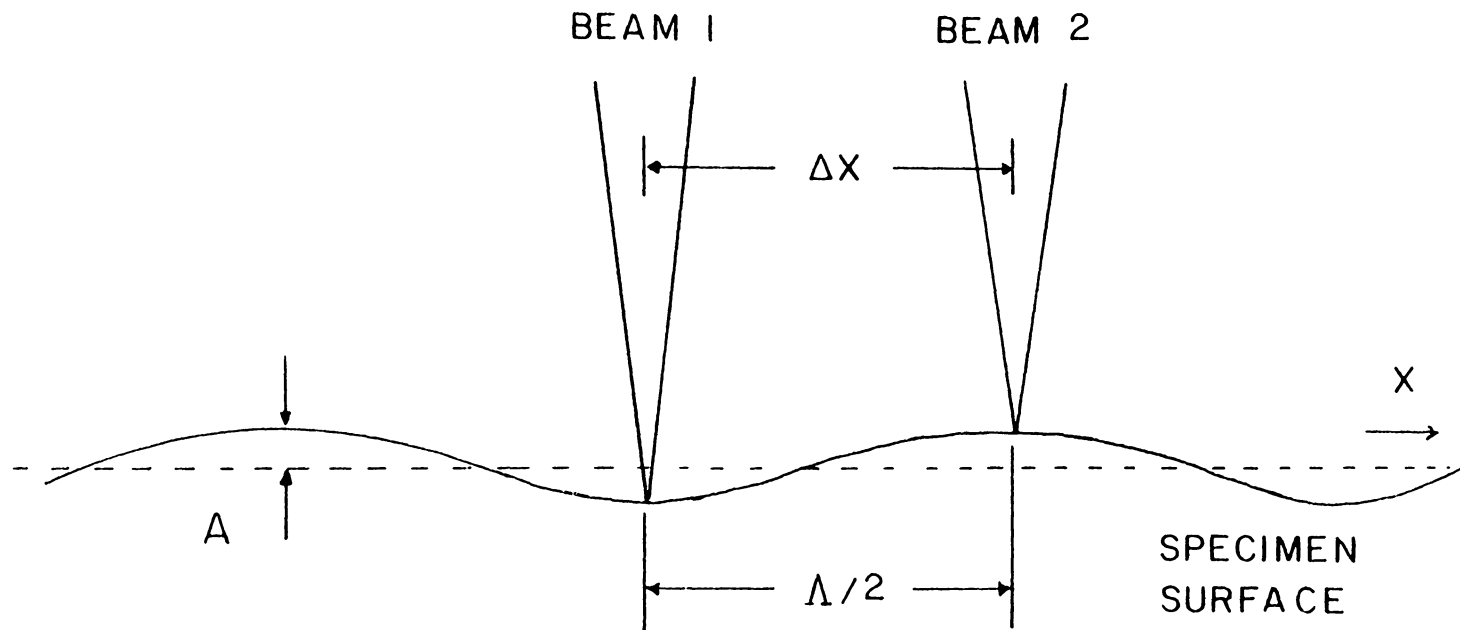


Figure 3.3. (a) The Ronchi grid transmitted intensity versus fringe position and (b) the position of maximum intensity change versus fringe modulation.



$$\Delta x = (2n + 1) \Lambda / 2$$

$$n = \{0, 1, 2, 3, \dots\}$$

$$\Lambda = 2\pi / K$$

Figure 3.4. Surface focus probe beam spot separation for maximum pathlength modulation [15].

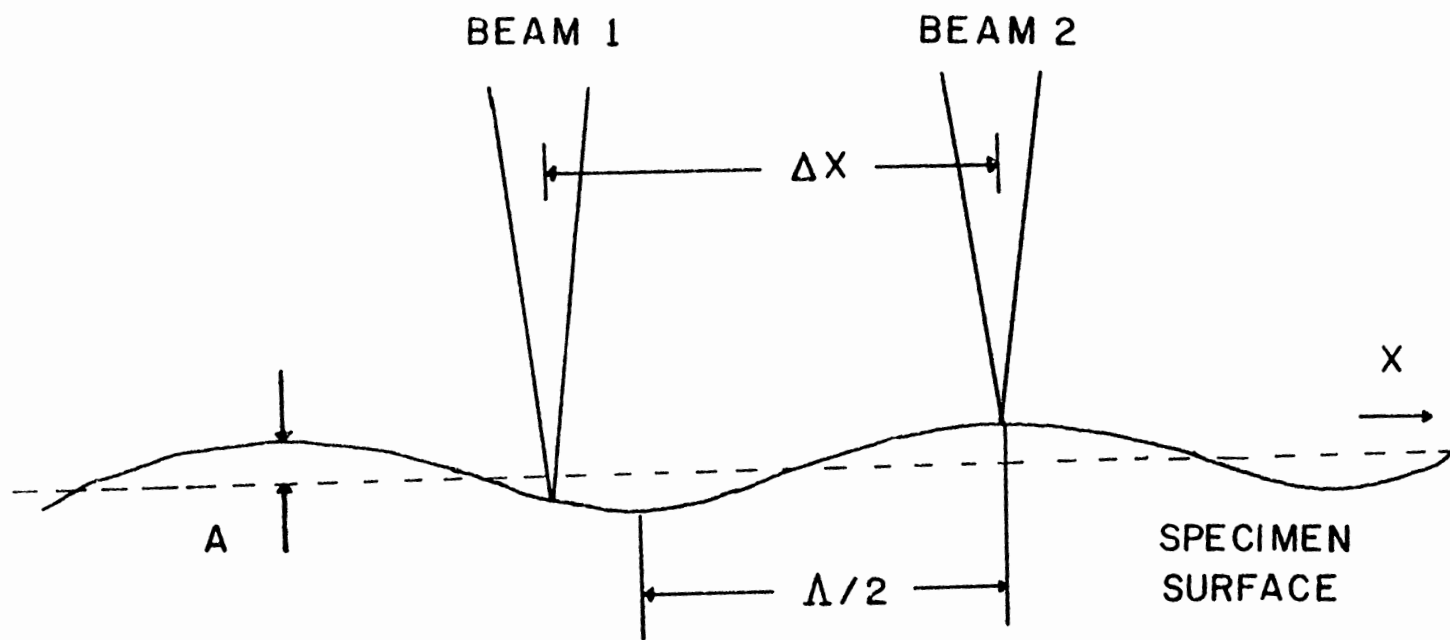


Figure 3.4b. Wideband Differential Interferometry Probe Geometry.



$$\delta = \delta_a \cos \omega_a t \quad (3.21)$$

where  $\delta$  is the normal surface displacement,  $\delta_a$  is the peak displacement, and  $\omega_a$  is the acoustic radian frequency. Referring to Figure 3.4, the two optical beams which are incident upon a surface modulated by an acoustic wave have maximum optical path difference of  $2 \delta \cos \alpha$ , where  $\alpha$  is again the incident angle of the probe beam propagation vector to the surface normal. Thus, the minimum detectable acoustical amplitude  $\delta_m$  for an ideal optical detector which is shot noise limited [15] is given by

$$\delta_m = (2eB/\gamma P_o)^{1/2} \lambda/8 \cos \alpha, \quad (3.22)$$

where  $e$  is the electron charge,  $B$  is the detector bandwidth and  $\gamma$  is the P-I-N photo diode sensitivity given in amperes per optical watt. For the case of probing at an optimal angle of incidence, this technique is slightly superior to the knife-edge technique in sensitivity. However, it is less sensitive than either the Fabry-Perot interferometer or the piezoelectric contact transducers, both of which involve signal integration [5].

The optical system used by Palmer, et. al. [15], is illustrated in Fig. 3.5. Two equal intensity beams are obtained from the single Helium-Neon laser source ( $\lambda = 6328\text{\AA}$ ) by passing the +1 and -1 orders of a diffraction pattern through a mesh. The diffraction pattern is

formed by passing the expanded, collimated laser beam through a Ronchi ruling, H, then focusing the image onto an optical stop. The  $\pm 1$ st orders, after the stop, are gathered and recollimated by lens L4. The variable focal length lens formed by the combination of individual lenses L5 and L6 focuses the collimated beams onto the specimen surface with the desired separation,

$$\Lambda / 2.$$

The reflected beams are recollimated upon passing back through the varifocal lens. In order to separate incident and reflected beams, the incident beams are passed through one half of the lens which allows the reflected beams to propagate through the other half and to be redirected by mirror M onto the Ronchi grid. In this recollimated region of beam overlap, the interference pattern imaged on the Ronchi ruling is spatially filtered, producing an intensity modulated field which is focused onto the detector by lens L7.

Work due to Jablonowski derives the bandwidth versus surface point probe beam separation distance for differential systems of Palmer's type [23]. For a separation distance  $\Lambda/2$  of the surface probe beams giving maximum sensitivity to an acoustical wave of frequency  $f_0$ , the bandwidth plot given in Figure 3.6a can be derived. The

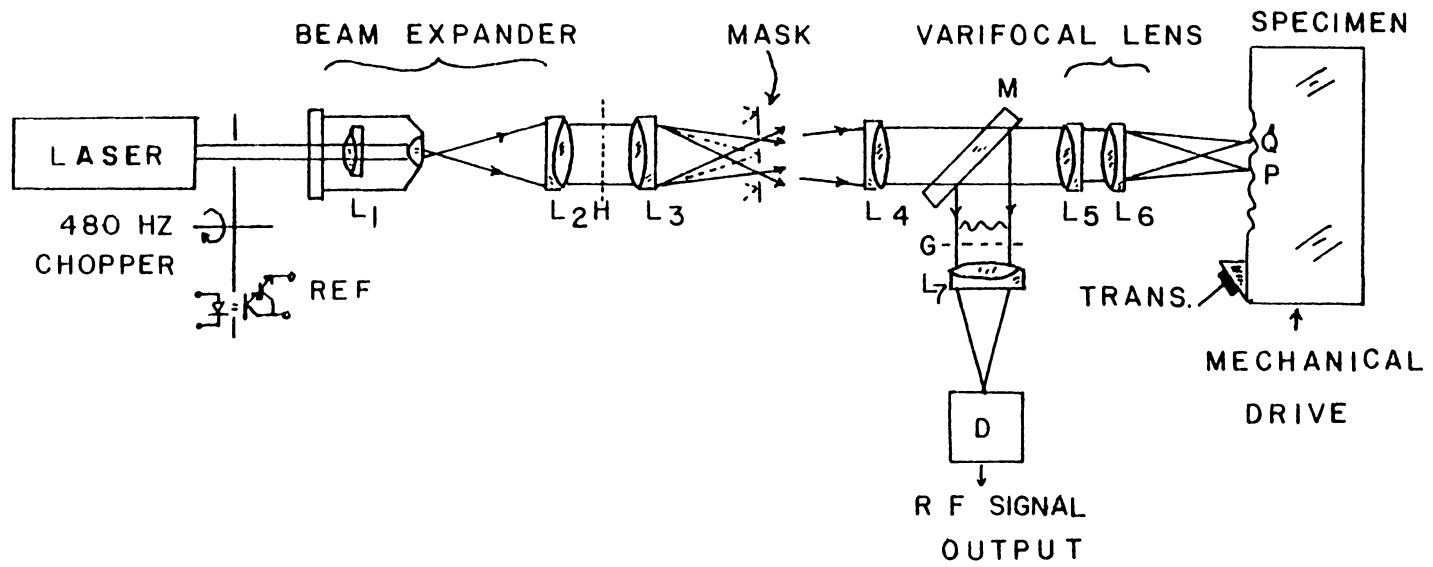


Figure 3.5. Optical set-up for differential interferometer [15].

nonlinear frequency response necessitates post-detection signal analysis to achieve a flat response for broadband measurements. Many digital data acquisition systems offer signal conditioning packages of this type making broadband detection feasible. By extending the separation distance between probe beams to one and a half wavelengths,  $d = 3 \lambda/2$ , the bandwidth pattern shown in Figure 3.6b can be achieved. The sensitivity has become much narrower which allows increased sensitivity to selected frequency bands. The effect is more pronounced in Figure 3.6c with an optical beam separation of  $5 \lambda/2$ . The inclusion of the repetitive sensitivity ranges does complicate data analysis unless adequate filtering is included in the detector electronics. In general, by careful consideration of the frequency spectrum of interest, either broadband or selective filtering can be accomplished by variation of the point probe separation.

The differential interferometer has an upper useful frequency related to the lower limit of the physical probe size on the specimen surface. The approximate waist diameter of a collimated plane wavefront of diameter  $d$  focused

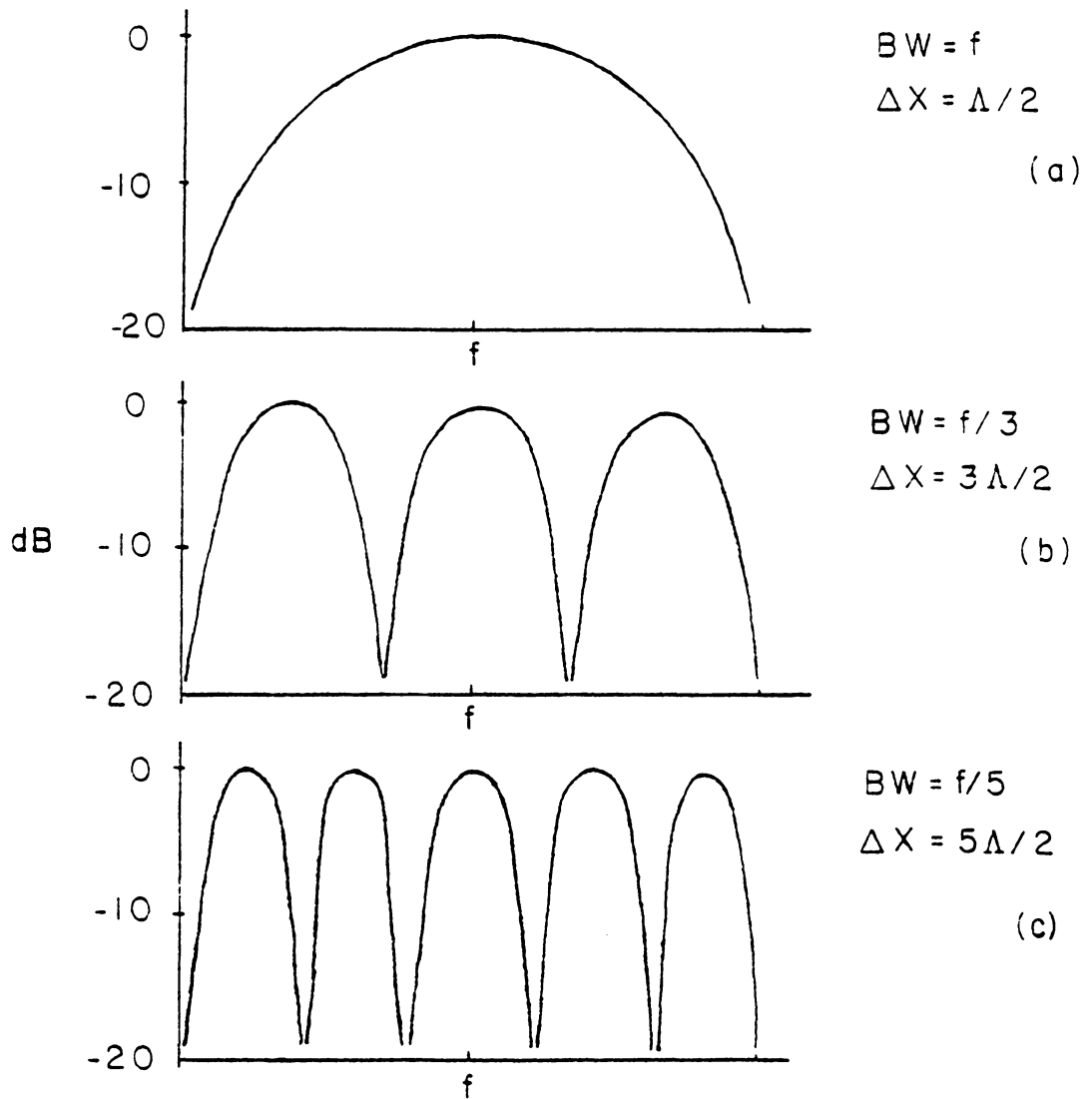


Figure 3.6. Sensitivity bandwidth plots of the differential interferometer for various focus spot separations [23].

by a lens of focal length  $L$  is given by [24]

$$\omega_0 = \frac{L\lambda}{\pi d} \quad (3.23)$$

where  $\omega_0$  is the waist diameter and  $\lambda$  is the optical wavelength. As the focus spot diameter approaches same the order of magnitude as that of the SAW wavelength, surface displacement averaging over the surface wave increases degradation of the sensitivity due to reduction of fringe modulation. The surface effect is diagrammed in Figure 3.7. In the limit where the spot diameter  $s$  at the surface is equal to the SAW wavelength  $\Lambda$ , the net signal modulation is zero. If the focus spot diameter is larger than the wavelength, some net fringe modulation can be realized. However, the diffraction effects due to the now non-negligible surface corrugation must be considered. Therefore, for all practical applications of the differential interferometer, the focus point diameter should remain less than ten percent of the surface wavelength being interrogated. The absolute upper limit is given by equation (3.23) where  $s$  is equal to  $\Lambda$ .

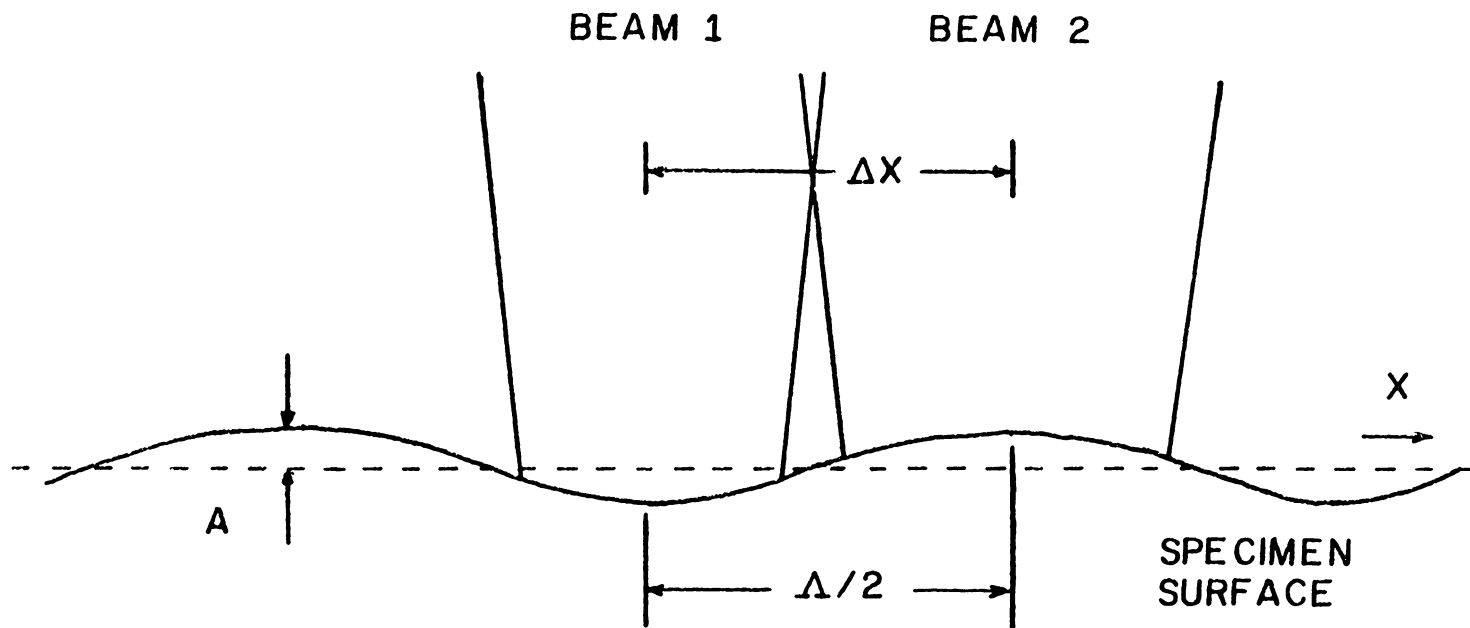


Figure 3.7. Averaging effect of small wavelength SAW.

Related to the frequency limitations just discussed, the differential interferometer has an insensitivity to misfocusing when not working near the upper frequency limit [15]. The effects of misfocusing are not significant if the surface spot diameter is less than one tenth of a surface wavelength. Long focal length lenses focus collimated beams into slowly contouring beams in the Fourier plane with somewhat larger waist diameters than shorter focal length lenses. Thus if the larger waist size of the focal beam can be tolerated, the smooth transition of the converging beam will allow reasonable tolerance in misfocusing.

### 3.2. DETECTION LIMITATION OF THE DIFFERENTIAL INTERFEROMETER

The two beam differential interferometer system is susceptible to amplitude errors for SAW propagation at an arbitrary angle with respect to the focused beam spot points as shown in Figure 3.8 [25]. Here, the detected amplitude is the amplitude component parallel to the focus points. This component is given by  $A_m = A_s \cos\theta$ , where  $A_m$  is the modulating amplitude,  $A_s$  is the SAW amplitude and  $\theta$  is the angle between the SAW propagation vector  $k$  and the



chord connecting the focus points. Experimental data of detected amplitude as a function of  $\theta$  is given in Figure 3.9 [25]. One approach to obtain a calibrated measurement of continuously generate SAW amplitude is to simply rotate the interferometer for maximum signal output. However, for transient pulse detection this is impractical because the location of the acoustic source, for example an acoustic emission, is seldom known prior to signal detection. Accurate, instantaneous resolution of transient SAW amplitude thus requires the detection of motion components both parallel and perpendicular to the chord connecting the focused laser spots. This is accomplished in the dual differential interferometer by the introduction of a second, independent interferometer with foci along a line oriented perpendicular to the connecting chord of the first pair.

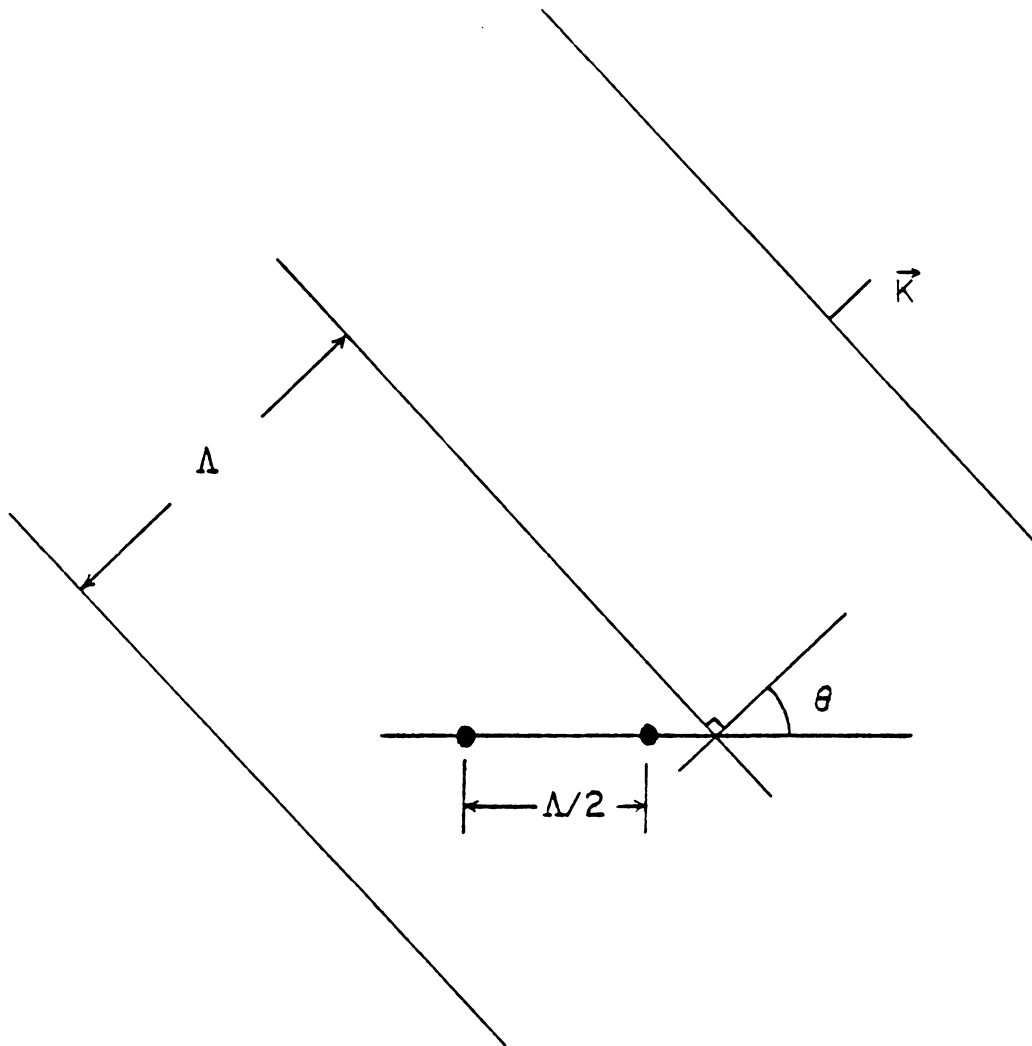


Figure 3.8. Angular sensitivity of the differential interferometer.

#### IV. THE DUAL DIFFERENTIAL INTERFEROMETER

##### 4.1. THEORETICAL DEVELOPMENT OF THE DUAL DIFFERENTIAL INTERFEROMETER

In the previous section, a major limitation of the differential interferometer utilized by Palmer, Claus and Fick was noted for the calibrated detection of transient surface acoustic waves, waves such as those generated by acoustic emission sources. The amplitude as a function of the incident angle of a SAW to the differential interferometer focus spots was shown to be

$$A_m = A_s \cos \theta , \quad (4.1)$$

where  $A_m$  is the modulated amplitude perceived by the interferometer,  $A_s$  is the surface wave amplitude, and  $\theta$  is the angle formed by the SAW propagation vector  $k$  and the chord connecting the interferometer focus spot pair. One approach that was considered is the addition of a second differential interferometer, labeled B, to measure the amplitude component of the incident SAW perpendicular to the original interferometer pair, labeled A, as shown in Figure 4.1 [26].

By positioning the interferometer surface spot pairs in the crosshairs configuration shown, two independent output

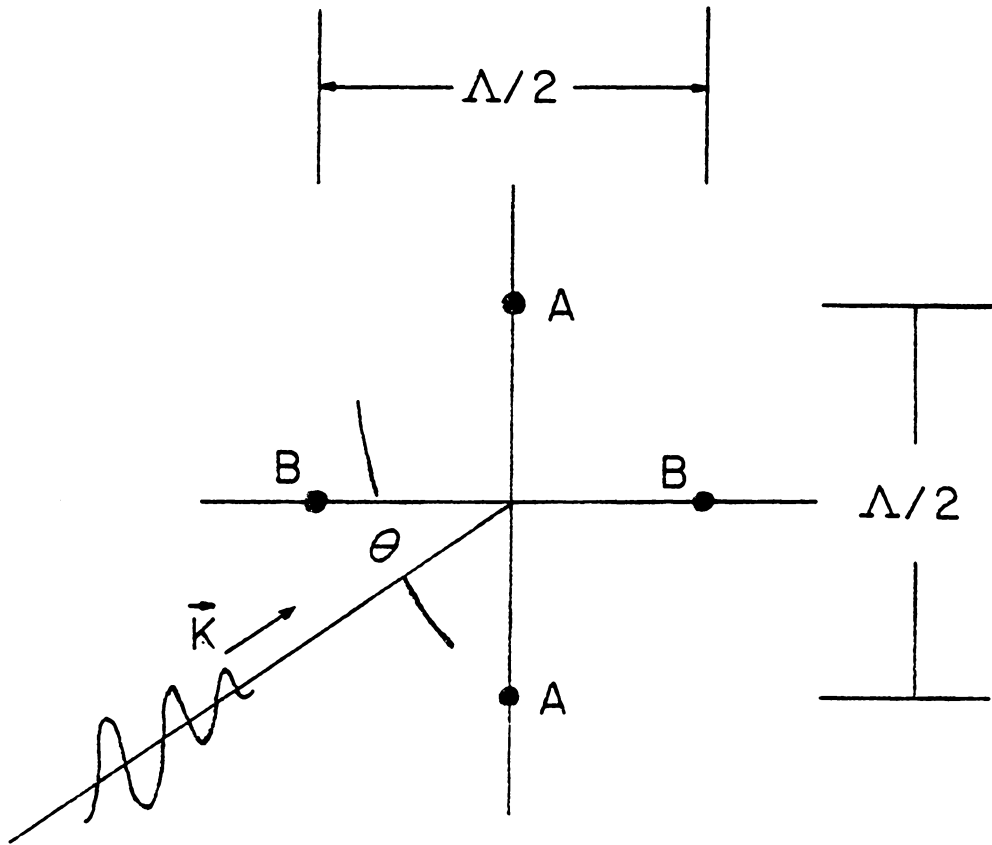


Figure 4.1. Dual interferometer focus point geometry [27].

signals may be obtained which are related to the corresponding perpendicular components of the amplitude of a wave propagating arbitrarily to the surface coordinate system determined by the interferometer. Choosing a coordinate axis along the A interferometer spot pair chord, a SAW propagating at an angular orientation of  $\theta$  ( $0^\circ \leq \theta \leq 90^\circ$ ) to this pair generates an output signal

$$A_B = A_S \cos \theta . \quad (4.2)$$

This signal is identical to the signal generated by the single interferometer already developed. Now, in addition, the interferometer produces a signal

$$A_A = |A_S \sin \theta| \quad (4.3)$$

which is the amplitude component parallel to the B interferometer spot pair. Additionally, the simultaneous outputs can be solved uniquely for the absolute amplitude  $A_S$  and for the propagation angle  $\theta$  in addition [26]. The determination of  $\theta$  with respect to the interferometer coordinates is an important advantage in locating acoustic emission sources. Unfortunately, the SAW  $k$  vector direction cannot be determined.

The equidistant placement of each focal point from the geometric center of the interferometer's surface configuration has the limitation that one forty-five degree orientation cannot be distinguished from the other. This

degeneracy can be resolved by placing the second interferometer pair unequally from the geometric center as shown in Figure 4.2. In this new configuration, interaction of the incident SAW should occur at distinct instances of time with each interferometer pair for the forty-five degree case.

#### 4.2. OPTICAL CONFIGURATION OF THE DUAL DIFFERENTIAL INTERFEROMETER

The determination of SAW amplitude and propagation orientation on a substrate could be accomplished by implementing two, completely distinct interferometers. The disadvantages of this approach were the joint systems' bulk, achieving proper alignment, and adjustment for sensitivity to particular SAW frequencies and bandwidth. Instead, a consolidated system was designed using one monochromatic laser source and the appropriate optical hardware for generation of four optical probe beams [26]. The separation of the four beams into two non-interacting pairs was achieved by orthogonally polarizing the interferometer pairs as shown in Figure 4.3. Since orthogonal polarizations can be separated by optical filtering, both pairs are transmitted through common optics and later separated for non-interactive measurements. This con-

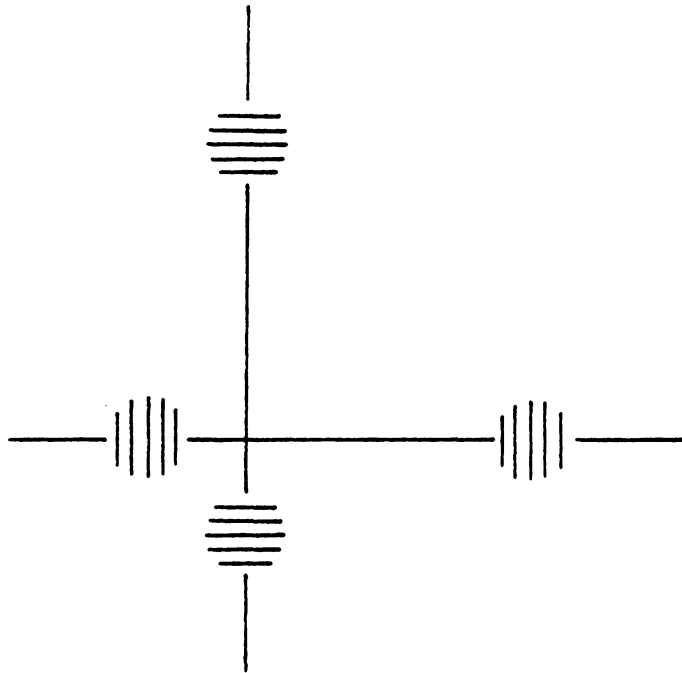


Figure 4.2. Focus points repositioned for SAW orientation ambiguities.

densed the optical component requirements and allowed the system to operate in an integrated manner.

The dual differential interferometer system first generates two pairs of parallel beams having a forty-five degree polarization angle with respect to the horizontal as shown in Figure 4.4. The initial polarization angle of the light source is obtained by rotating a linearly polarized Helium-Neon laser appropriately. As shown, the two pairs of beams are split at right angles to each other upon their exit from beamsplitter B2. A dove prism, DP, mounted at a forty-five degree angle to the horizontal is inserted into the path of one pair. This rotates the orientation of the pair by ninety degrees so that they are now vertical to one another, but does not affect the pair's polarization. Both pairs are then made incident onto a polarizing beamsplitter, B3, which aligns and positions both pairs onto the varifocal lens. This alignment also results in the orthogonal polarization of one beam pair with respect to the other and in their comparable intensities.

The two pairs of orthogonally polarized beams propagate toward the varifocal lens in a quasi-parallel direction. Due to the size of the polarizing beamsplitter, the beams had to be slightly divergent to achieve the separation on



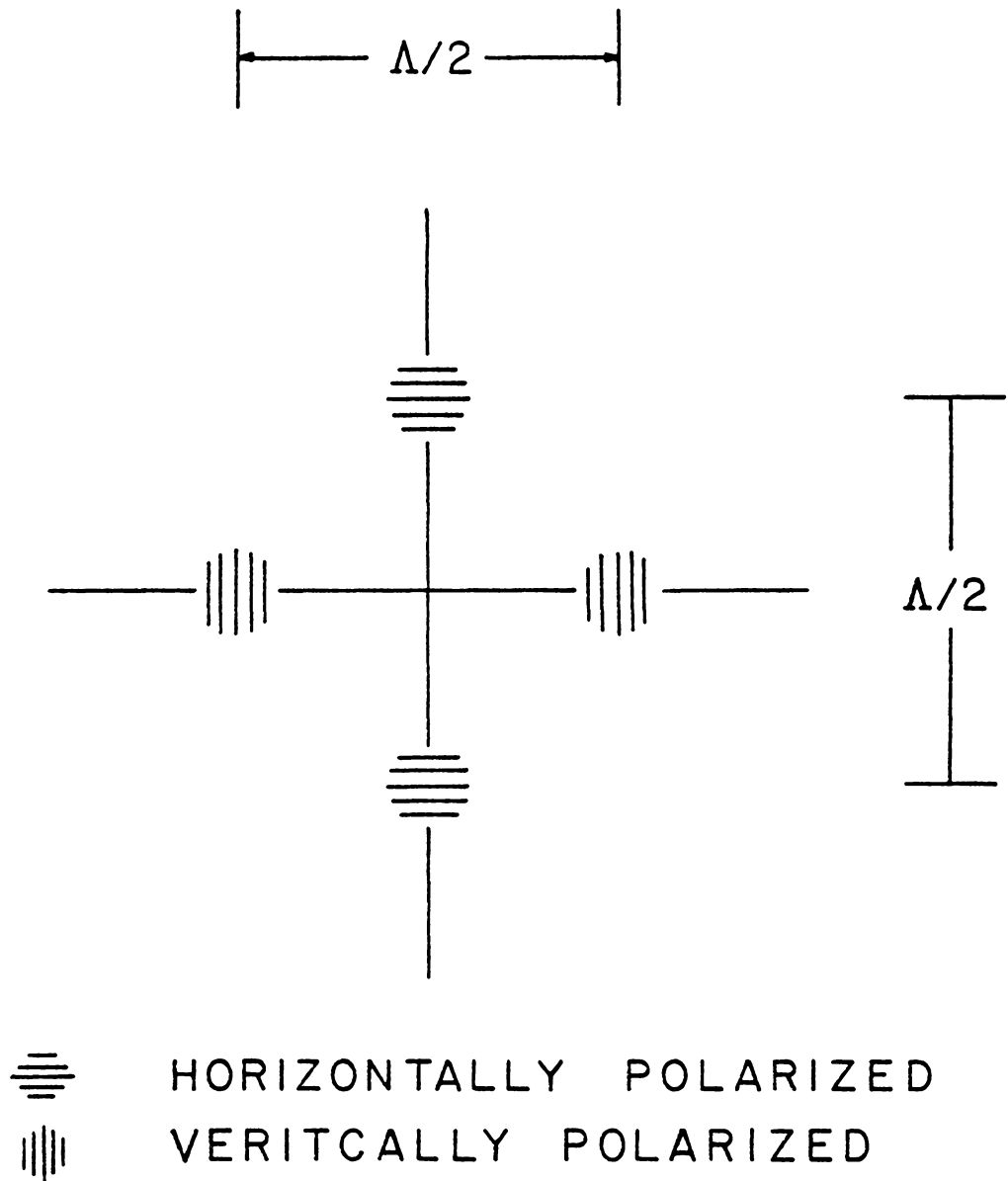


Figure 4.3. Orthogonal polarization of beam pairs [27].

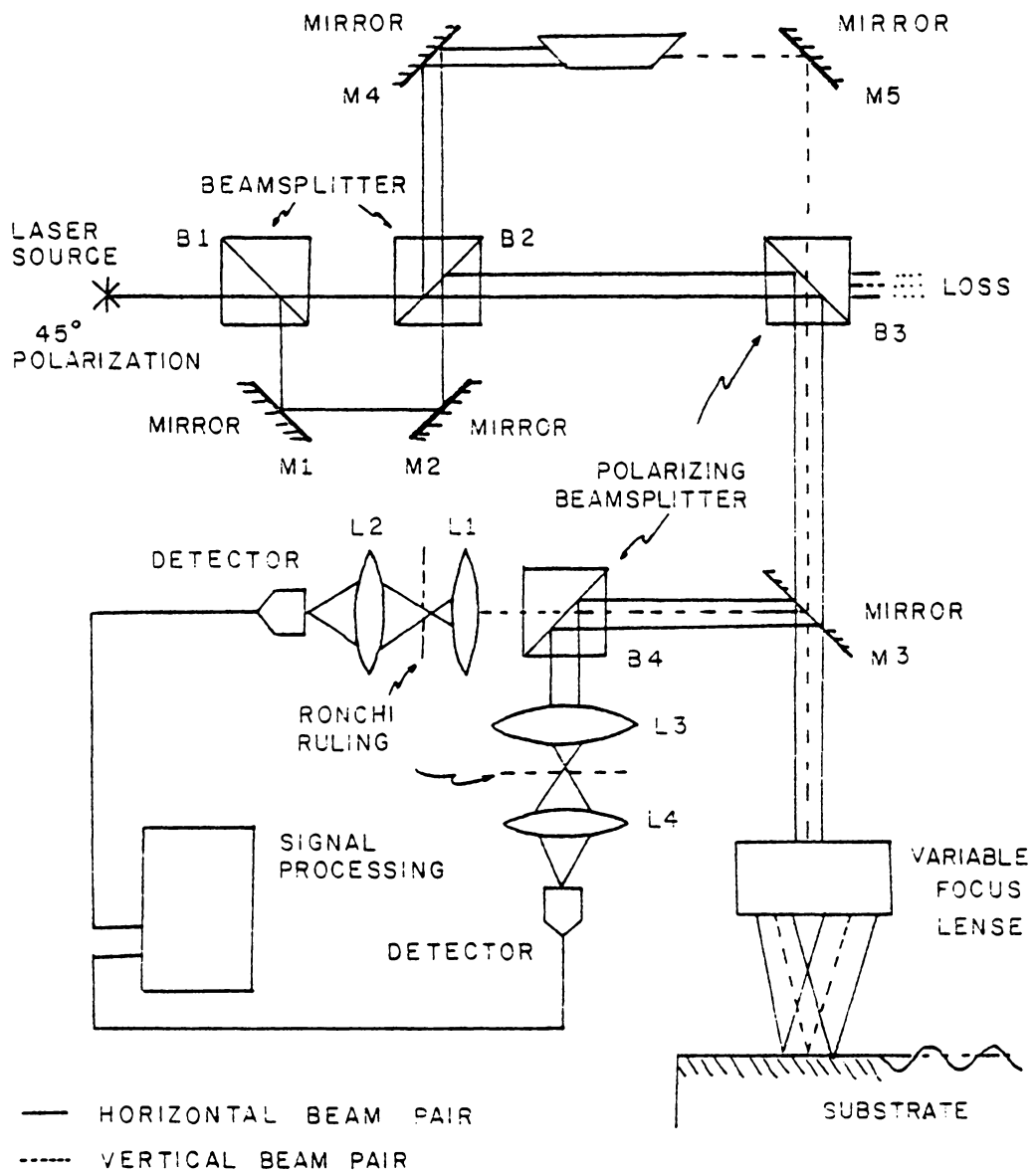


Figure 4.4. Optical configuration of the dual differential interferometer [27].

the substrate that was desired for frequencies 2.25 MHz and below. The varifocal lens could then achieve variable separation distances of a few tenths of a millimeter to several centimeters. The reflected beams were directed towards detection electronics by mirror pairs, M3, which reflect the diverging beams into a polarizing beamsplitter, B4. The polarizing beamsplitter B4 separates the reflected pairs and each pair is individually expanded, spatially filtered, and measured for fringe modulation. A United Detector Technology PIN 020A photo diode was used for signal detection.

Both interferometer beam pairs may be expanded and refocused onto the surface by the variable focus lens system. With this lens system, the separation of the focused spots can be varied as noted before. However, beam spot separation may also be manipulated by separating the beams at the point of generation at the front of the system [26]. This is accomplished by translation of the mirror pair, M1 and M2, adjacent to the beamsplitter B1 and B2. Again the size of the optical components limits the range of separation to small increments as compared to the variable focus lens system.

There is an obvious difference between the interferometer system used by Palmer et al. and the dual interferome-

ter described here. The difference is the use of laser pencil beams as opposed to the enlarged, collimated beams of Palmer's system. The effect of this difference is to require the diverging, reflected beams from the substrate to be redirected towards the beamsplitter B4 by two, mechanically independent mirrors for each pair. This one feature allows acoustical noise to enter the system through the mechanically decoupled mirrors. The reason for implementing the system with pencil beams is that of the size of the optical components which would not allow enlarged beams. The major, limiting factor in this regard was the size of the dove prism, only one centimeter by one centimeter. Despite this size limitation, the application of theory as defined for the Palmer differential interferometer applies equally well to the dual differential interferometer.

## V. CONSTRUCTION OF THE DUAL INTERFEROMETRIC SYSTEM AND EXPERIMENTATION

The laboratory trials of the dual differential interferometer emphasized the experimental investigation of the SAW detection design concepts. The initial goal was to determine whether each interferometer separately retained sufficient absolute sensitivity to allow SAW detection despite the significant dispersion caused by the numerous surfaces in the optical system. As part of this first experiment, the relative sensitivity of the two interferometers also would be determined to allow the correction of any inequality in system gain. This is of specific importance when both signal channels are used simultaneously. The second goal would be to measure the resolution of the dual interferometric system in identifying the location of a known SAW source. Here the relative sensitivities of the two interferometers must be identical since a mismatch in system gain would produce a source location error during data analysis. Finally, the interferometer probe beam pattern should be arbitrarily oriented on the substrate surface for the detection of random SAW transients excited on the substrate. The outputs of each interferometer would be post detection ana-

lyzed for signal amplitude and surface wave propagation orientation.

The system was constructed as shown in Figure 5.1 (reprinted from Figure 4.4 ) on a two meter by three meter optical table which is acoustically isolated from the floor by four air suspension columns. Although the effect of the mechanical isolation supports was significant in reducing vibrational noise, some low frequency noise caused by spurious floor motion was still coupled through the legs to the table. Figure 5.2 graphs frequency versus attenuation for the optical table. Since output signals in the interferometric system are functions of the absolute relative positions of the optical beams, the system sensitivity to acoustical noise was appreciable due to the mechanical instability of the supports used for mounting the individual optical components. The mechanical attachment of the supports to the table by magnetic bases and triangular optical mounts was sufficiently firm. However, the suspension of heavy optical hardware on 1.27 cm diameter mounting posts extending from these bases allowed mechanical oscillations with respect to the table generated by audible and inaudible noises including speech and movements around the table.

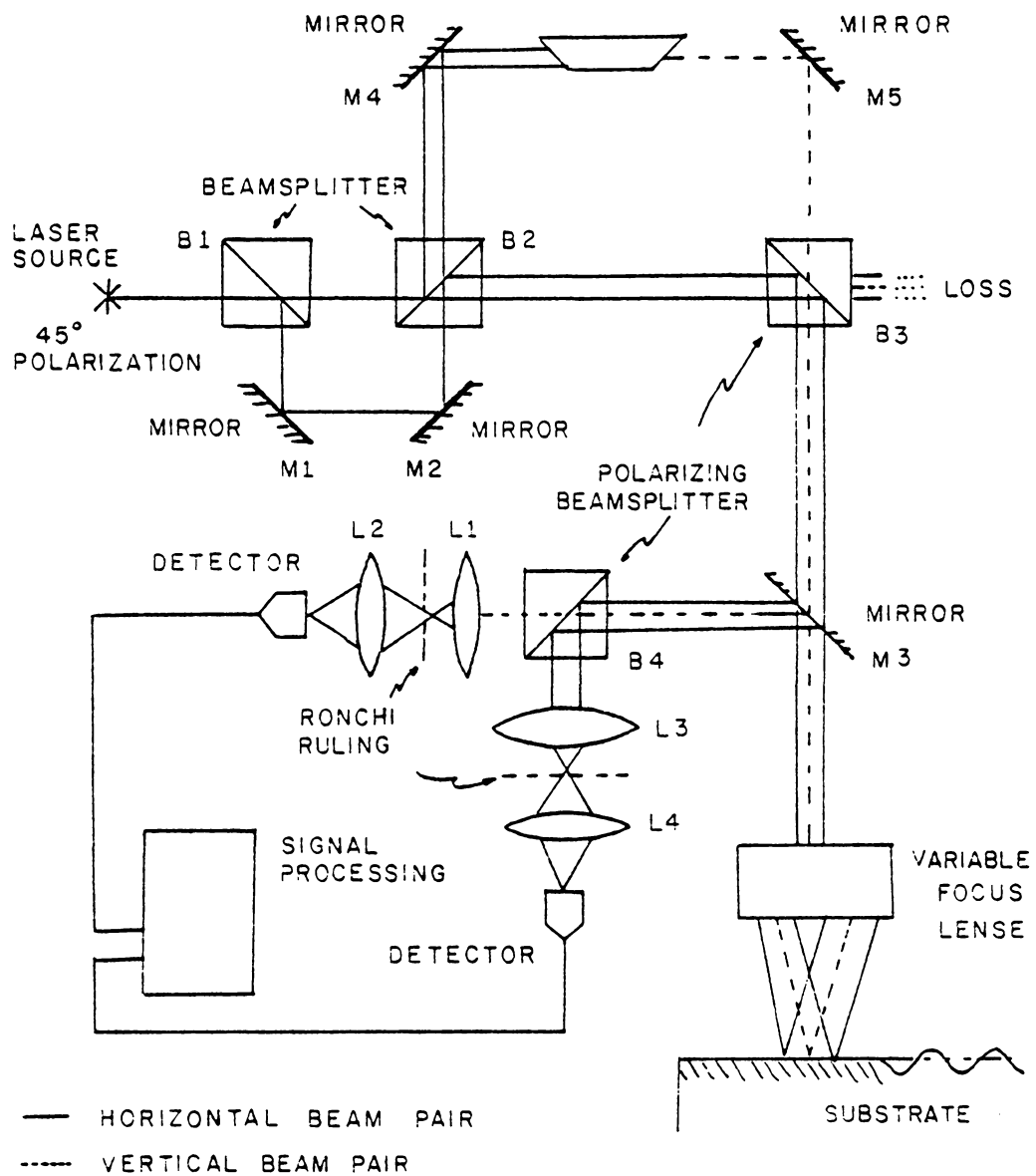


Figure 5.1. The experimental optical set-up of the dual differential interferometer [27].

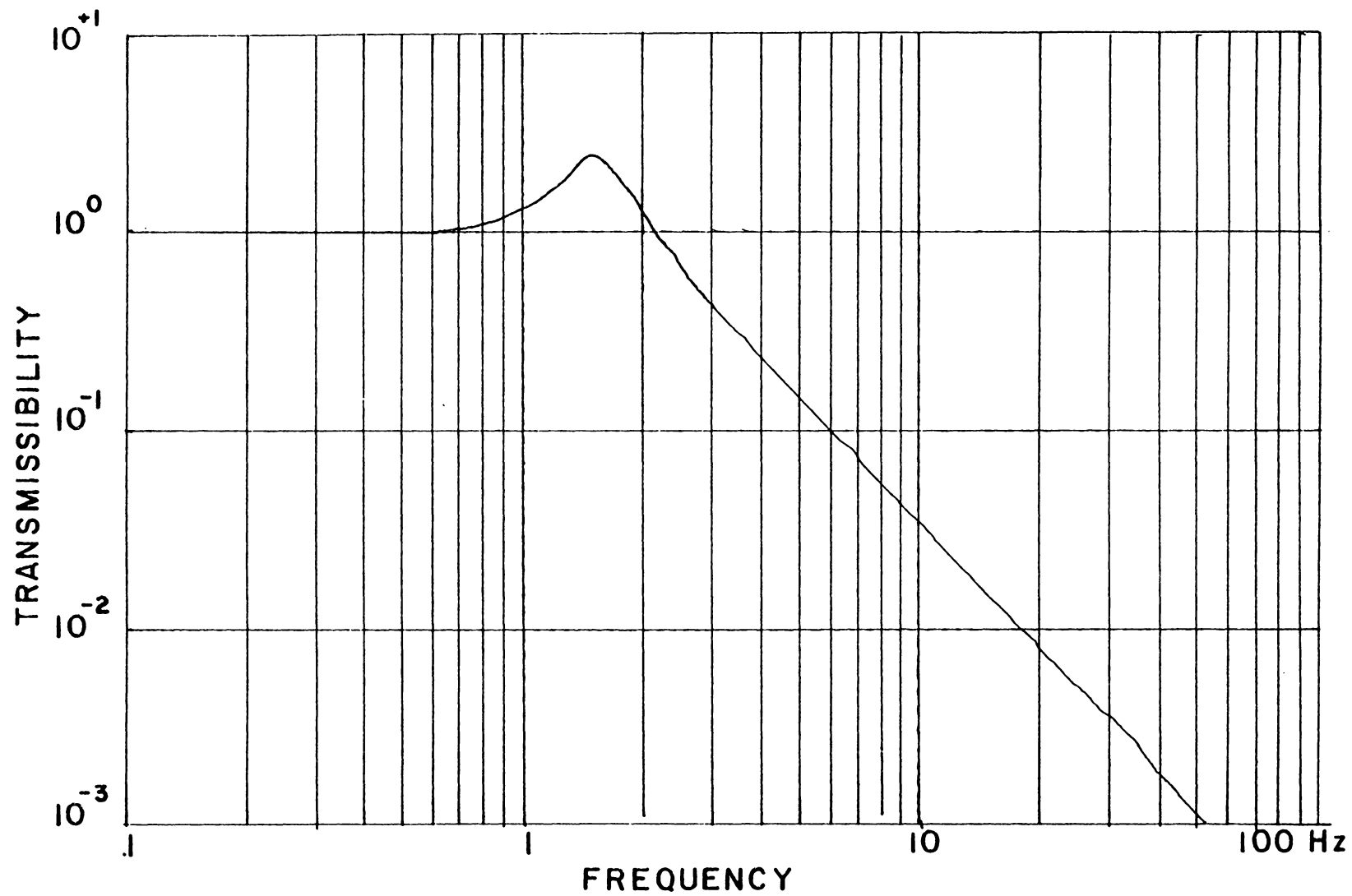


Figure 5.2. Acoustic sensitivity for the NRC Research optical table [28].



The optical system was aligned by careful autocollimation to insure the horizontal propagation of the laser beam parallel to the surface of the optical table and right angle reflections of the split beams from all reflecting surfaces. Initially, the beams were superimposed for alignment and later separated to give the desired probe beam pattern on the substrate. Once aligned, the system could be easily calibrated for acoustic frequencies from kilohertz to megahertz and for relative interferometric beam pair patterns. Beam pair separations were changed by adjustment of either the focal length of the variable focus lens or the parallel displacement of mirrors M1 and M2 to the optical path as shown in Figure 5.1. Beam pair orientations were made by the angular adjustment of the polarizing beamsplitter B3 shown in Figure 5.1 with respect to the propagation path on the substrate. Lastly, the remaining optical components necessary for focusing the output optical beam onto the active area of the photodiode detector were aligned.

To achieve a desired probe beam separation on the surface while maintaining sharp focal points required the source beams to be diverging upon exit from the beamsplitter B3. The focusing lens could then be positioned to simultaneously obtain surface spot separation and small

focus point diameters. This geometry presented some difficulty in alignment at the detector because the diverging beams cannot be simply expanded to form overlapping regions. The differential propagation distance through the entire optical system for each unmodulated beam of a polarized pair changed the laser beam wavefront geometry, making the planar wavefront assumption no longer valid. The spherical nature of the beams and their divergence with propagation distance produces extremely fine interference lines when the beams are expanded. The interference pattern generated was thus too faint to detect even visually. A long propagation distance to the point of recombination helps to negate differences in propagation distance of any two beams. The ratio of the difference in propagation to total propagation length decreases significantly as the propagation pathlength increases assuming no change in the pathlength difference. Thus the beams were individually reflected from mirrors to a single lens approximately five meters from the mirrors. Also, this configuration allowed all of the incident light in both beams to be utilized for interference. The fringes became visible. The fringes were still closely spaced due to the small angle of convergence of the beams from the mirrors and their spherical wavefronts.

Fringe translation was easily detectable for motions induced in the system by background noise and vibrations. Gross oscillations such as those produced by mechanically rotating the experimental substrate, a glass mirror, could also be seen. However, these system reactions to physical surroundings did not produce the erratic behavior generally observed using high sensitivity interferometers. This observation was confirmed by further experimentation. Separation of the signals obtained for the two axes was observed for mechanical angular rotations of the substrate. A pulse obtained from one such rotation is shown in Figure 5.3. The relative sensitivity of each interferometer could not be determined due to the large amplitude of the motions. To test the system sensitivity to low amplitude CW ultrasonic waves, a Harasonic G204 2.25 MHz piezoelectric variable wedge surface wave transducer was attached to the substrate with a mineral oil fluid layer as a mechanical coupler. The propagation direction of the transducer was aligned so maximum sensitivity could be obtained by one interferometer. The transducer was pulsed with a single cycle of 2.25 MHz and the detector output was fed into a Tektronics 506A 50MHz oscilloscope synchronized to the timing of the transducer pulse. Unfortunately, regardless of system adjustments, no indication of

the propagating SAW transient could be observed. However, the presence of the SAW on the substrate was verified by observations using a second timed piezoelectric transducer which was mounted on the substrate surface.

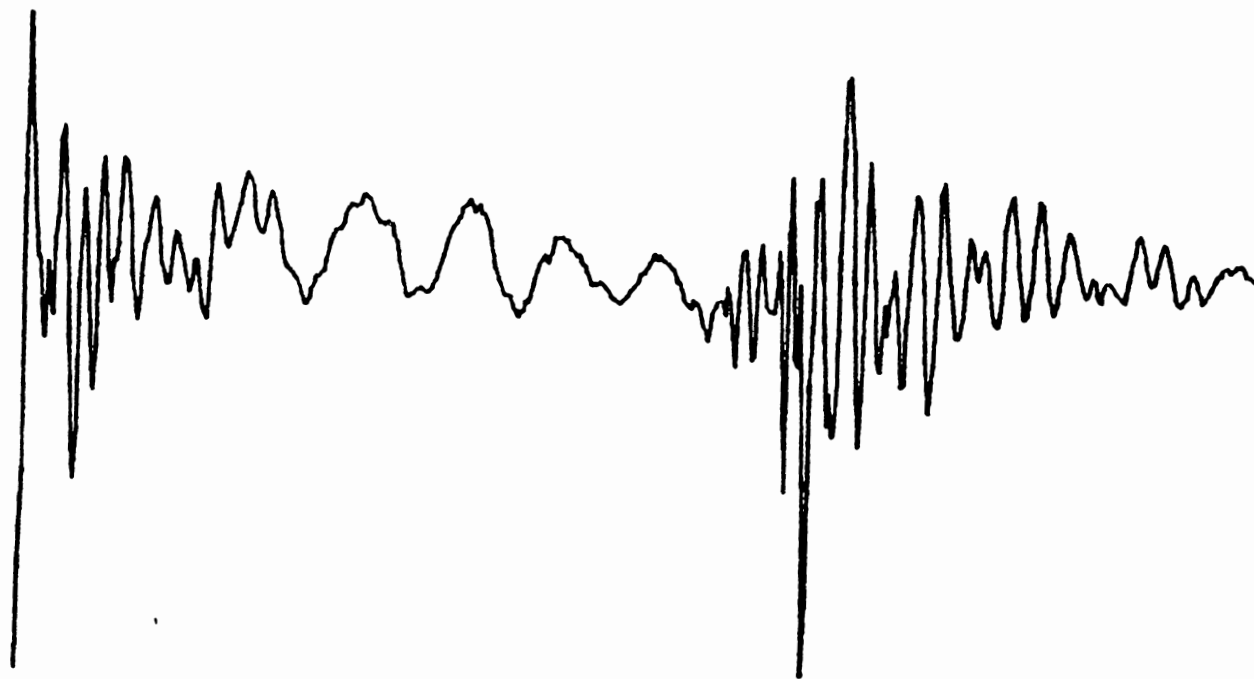


Figure 5.3. Low frequency, large amplitude single channel acoustic signal.

## VI. CONCLUSIONS AND FOR FURTHER CONSIDERATION

The dual differential interferometer remained insensitive despite modifications to the optical arrangement both at the surface and in the detection scheme. Unfortunately, only simple optical detection schemes could be employed due to the severe loss of optical power. The most difficult problem encountered was the divergence of the optical beams after reflection from the substrate surface. Due to the physical size of the optical components, divergence of the beam pairs was necessary to obtain desired focal point separation and focal spot size. The divergence was too severe to allow simple expansion of each beam to form a region of beam overlap. The resultant optical power in this interference region was too weak for spatial demodulation and optical detection. Another approach was the recombination of the beams using a beam-splitter. Again, however, the resulting optical output was too weak for detection. To minimize convergence angle and also to reduce the effect of each beam pair's static optical pathlength distance, inherent in the system, the beams were directed toward a lens sufficiently large to contain the beams approximately six meters away. On the image side of the lens, the interference fringes were discerna-

ble, however, they were narrow and low in intensity. The Ronchi ruling placed in the optical path of the overlapping beams created a circular image due to the slight curvature of the optical interference pattern. The Ronchi grid reduced the available optical power by one half, but this was conceivably offset by utilizing all available optical power of both beams. The center of the image was focused onto the photodiode. As previously discussed, however, the system remained insensitive to surface waves.

In addition to the combined problems of pathlength difference and diverging beams, several other contributing factors were present. One was the photodiode detector amplifier used with the system. The amplifier was broadband which caused the signal-to-noise at the 2.25 megahertz SAW signal to be drastically reduced. The sensitivity limits to which these optical detectors must be pushed almost necessitates the use of signal conditioning to separate detected signal from radiated noise of the laser and surface wave transducer drive electronics. These techniques were not applied. A related limitation is the low laser power available. Additional optical power would increase fringe intensity allowing greater photodiode excitation. Lastly, insufficient fringe modulation could be related to low coupling efficiencies of the wedge

transducers used for SAW generation. In addition, suspension of massive optical components on the 1.25 centimeter posts permitted the coupling of airborne and acoustically coupled building structural noise into the system. The resultant noise in fringe modulation could swamp the signal modulation.

Basic solutions to the dual differential interferometer's mechanical problems are to reduce the elevation of the entire system in order to reduce the moment of mass suspended on the component support posts. Direct mounting onto the optical table is the optimum solution. Improvement of other conditions such as laser power and SAW generation have obvious benefits.

More specific modifications to the optical system could be implemented for possible improvement to the overall interferometer system. For a reference, Palmer, Claus and Fick had much success by propagating both beams together in a single expanded, collimated beam for imaging onto the substrate surface [15]. By condensing the dual differential interferometer's four beams into a narrow packet, they may possibly be expanded and collimated and then focused onto the substrate as desired without the need to propagate them in a diverging pattern. Subsequent detection could then be performed in an analogous manner as



discussed for the two-beam differential interferometer. On the other hand, expensive optical components with the required dimensions to transmit large collimated beams could be substituted for the present components. The cost would be prohibitive, however.

A more elegant technique would be to use Fourier optics methods to generate the four probe points. Taking a sheet of aluminum flashing and punching the four probe points in a desired configuration, the image in the focal plane,  $G$ , of the flashing, illuminated from behind, will be the Fourier optical transform of the four point sources. As is true in general Fourier techniques, the inverse transform of  $G$  will generate  $g$ . Therefore, by exposing high density photographic film at  $G$  and developing it, the developed film may now be illuminated at  $G$  to produce in its Fourier plane (focal plane),  $g$ , the four probe points. By using the correct focal length lens between  $G$  and a substrate surface, the point probe pattern,  $g$ , of desired separation with small point probe dimension is obtained on the substrate.

The reflected intensity image in the Fourier plane would be a semblance of two perpendicularly oriented diffraction gratings. Modulation of the diffraction image for surface points would occur independently along perpen-

dicular axes in proportion to the related amplitude component of the surface wave. The exact relation between the reflected image and surface coordinates would be determined by the optical Fourier transform. Optical demodulation could still be accomplished by positioning a fringe width matching Ronchi ruling in the focal plane with lines parallel to the desired image axes. The input into the optical detector would be intensity modulated as before. The perpendicular component would be simultaneously removed.

## REFERENCES

1. G. S. Kino, "Nondestructive evaluation," *Science*, vol. 206, pp.173-180, October 1979.
2. R. V. Williams, Acoustic Emission. Bristol, England: Adam Hilger,Ltd., 1980, pp. 5-11.
3. R. W. Nichols, Acoustic Emission. London, England: Applied Science Publishers, 1976, pp.1-13, 51-54.
4. R. Kline, "Three-dimensional measurements of surface acoustic waves," unpublished.
5. G. I. Stegeman, "Optical probing of surface waves and surface wave devices," *IEEE Trans on Sonics and Ultrasonics*, Vol. SU-23, pp.33-63, January 1976.
6. R. L. Whitman and A. Korpel, "Probing of acoustic surface perturbations by coherent light," *Applied Optics*, Vol. 8, pp. 1567-1576, August 1969.
7. R. B. Thompson, "Noncontact transducers," 1977 IEEE Ultrasonics Symposium Proceedings (IEEE, New York, 1977) p. 74-83. (1977).
8. J. F. Martin and R. B. Thompson, "The twin magnet EMAT configuration for exciting horizontally polarized shear waves," 1981 IEEE Ultrasonics Symposium Preprint.
9. R. Adler, A. Korpel and P. Desmares, "An instrument for making surface waves visible," *IEEE Trans on Sonics and Ultrasonics*, vol. SU-15, p. 157, March, 1968.
10. G. Alers, M. A. Tennison, R. B. Thompson and B. R. Tittman, "Visualization of surface elastic waves on structural materials," *Ultrasonics*, vol. , pp. 174-177, July 1973.
11. R. M. De La Rue, R. F. Humphreys, I. M. Mason, and E. A. Ash, "Acoustic-surface-wave amplitude and phase measurements using laser probes," *Proc. IEE*, vol. 119, pp. 117-126, February 1972.
12. A. Alippi, A. Palma, L. Palmieri, and G. Socino, "Surface wave amplitude determination by optical techni-

que," *Lettre al Nuovo Cimento*, vol. 1, pp. 239-242, February 1971.

13. E. Hecht and A. Zajac, Optics. Reading, Mass.: Addison-Wesley, 1974, pp. 307-311.

14. C. H. Palmer, "Ultrasonic surface wave detection by optical interferometry," *J. of Acoustical Soc. of America*, vol. 53, pp. 948-949, March 1973.

15. C. H. Palmer, R. O. Claus, and S. E. Fick, "Ultrasonic wave measurement by differential interferometry," *Applied Optics*, vol. 16, July 1977.

16. I. A. Viktorov, Rayleigh and Lamb Waves. New York: Plenum Press, 1967, pp. 1-7.

17. B. A. Auld, Acoustic Fields and Waves in Solids, Vol. I. New York: John Wiley, 1973, pp. 1-134.

18. R. M. White, "Elastic surface waves," *Proc. IEEE*, vol. 58, pp. 1238-1276, August 1970.

19. G. W. Farnell, "Acoustic surface waves," *Topics in Applied Physics*, vol. 24, edited by A. A. Oliner, New York, Springer-Verlag, 1978, pp. 13-22.

20. H. L. Bertoni and T. Tamir, "Characteristics of wedge transducers for acoustic surface waves," *IEEE Trans on Sonics and Ultrasonics*, vol. 5a-22, pp. 415-420, November 1975.

21. B. A. Auld, Acoustic Fields and Waves in Solids, Vol. II. New York: John Wiley, 1973, pp. 190-199.

22. T. M. Turner and R. O. Claus, "Pulse-echo interface wave characterization of bolted plates," *IEEE Region 3 Conference (Huntsville, AL)*, pp. 484-486, April 1981.

23. D. P. Tablonowski, "Simple interferometer for monitoring Rayleigh waves," *Applied Optics*, vol. 17, July 1978.

24. A. E. Siegman, An Introduction to Lasers and Masers. New York: McGraw-Hill, 1971, pp. 312-321.

25. R. O. Claus and J. Cantrell, unpublished work.

26. T. M. Turner and R. O. Claus, "Dual differential interferometer for measurements of broadband surface acoustic waves," 1981 IEEE Ultrasonics Symposium (Chicago, IL), pp. 384-387, October 1981.
27. New Research Corporation Supply Catalog, 1980-1981.

**The vita has been removed from  
the scanned document**

A DUAL DIFFERENTIAL INTERFEROMETER FOR MEASUREMENTS  
OF BROADBAND  
SURFACE ACOUSTIC WAVES

by

Tyson M. Turner

(ABSTRACT)

A simple dual interferometer which uses two pairs of orthogonally polarized optical beams to measure both the amplitude and direction of propagation of broadband ultrasonic surface waves is described. Each pair of focused laser probe beams is used in a separate wideband differential interferometer to independently detect the component of surface wave motion along one direction of the surface. By combining the two output signals corresponding to both components, the two dimensional surface profile and its variation as a function of time may be determined. Although the system has an optically adjustable -3db acoustic bandwidth of more than two decades (eg. 30kHz to 3MHz for acoustic emission measurements) and may detect peak displacements in the sub-Angstrom range, it is designed to be insensitive to low frequency specimen translation. Potential applications in nondestructive evaluation are discussed.